A STUDY OF MICROWAVE REMOTE SENSING OF NATURAL MEDIUM USING RADIATIVE TRANSFER THEORY AND RELAXED HIERARCHICAL EQUIVALENT SOURCE ALGORITHM

LUM CHAN FAI

MASTER OF ENGINEERING SCIENCE

LEE KONG CHIAN FACULTY OF ENGINEERING AND SCIENCE

UNIVERSITI TUNKU ABDUL RAHMAN

JUNE 2018

A STUDY OF MICROWAVE REMOTE SENSING OF NATURAL MEDIUM USING RADIATIVE TRANSFER THEORY AND RELAXED HIERARCHICAL EQUIVALENT SOURCE ALGORITHM

By

LUM CHAN FAI

A dissertation submitted to the Department of Electrical and Electronics Engineering,
Lee Kong Chian Faculty of Engineering and Science,
Universiti Tunku Abdul Rahman,
in partial fulfilment of the requirements for the degree of
Master of Engineering Science
June 2018

ABSTRACT

A STUDY OF MICROWAVE REMOTE SENSING OF NATURAL MEDIUM USING RADIATIVE TRANSFER THEORY AND RELAXED HIERARCHICAL EQUIVALENT SOURCE ALGORITHM

Lum Chan Fai

Microwave remote sensing has become increasingly important in the study of the earth terrain. It provides a great, convenient, long-term monitoring, safe and fast solution to retrieve important information in a medium without the need for physical data collections at dangerous places. Synthetic Aperture Radar (SAR) images generated by the microwave remote sensing sensors contain lot of useful information needed for research works such as snow depth, snow water equivalent (SWE), surface roughness and others. These kinds of information are interrelated and can be estimated using a scattering theoretical model once some measurements are known. Backscatter theoretical model using analytical solution developed based on radiative transfer (RT) theory has been famous for its accuracy and been widely used to study the earth terrain like snow, sea ice and vegetation. Basic shapes like sphere, disk, cylinder and ellipsoid are frequently used to represent the scatterers inside a snow or vegetation mediums. Due to the limitation of basic shapes used by the existing radiative transfer theoretical model, to further understand and study the interactions between microwave and a medium which scatterers are irregular shape become difficult with existing backscatter model. As shown by some research works, the scatterers inside a snow medium could be in non-spherical form due to the metamorphism and sintering process. Thus, a new radiative transfer theoretical model using numerical solution could allow the use of non-spherical scatterers to better represent the actual shape of real scatterers inside a medium and helps researchers understand better the interactions between microwave and a medium. This study focuses on developing a new backscatter model which incorporates with numerical solution to provide the capabilities to simulate the irregular shape of scatterers. The theoretical analysis is performed to study the performance and accuracy of the newly developed theoretical model and simulation results are compared with ground truth measurement data. Shapes like cylinder, peanut and sphere are simulated and compared using different frequencies, incidence angles, layer thicknesses and volume fractions. Ground truth measurement data collected from Antarctica and the NASA’s Cold Land Processes Field Experiment (CLPX) are compared with the simulation results using three different shapes of scatterers. The good matching of results are obtained and there are different scattering patterns between different shapes of scatterers that are simulated. The results show that in some cases, non-spherical scatterers can have better match as compared to spherical scatterers. A new RT theoretical model that incorporates the relaxed hierarchical equivalent source algorithm (RHESA) model to give the capability to simulate arbitrary shape of scatterers has been developed and studied.

ACKNOWLEDGEMENT

First and foremost, I would like to take this opportunity to thank my supervisor, Prof. Ir. Dr. Ewe Hong Tat, and co-supervisor, Mr. Lee Yu Jen, for their guidance and advice throughout the research of this study. I would like to thank my supervisor again for his kindness, patient and time during the preparation of this dissertation. Special thank to my external co-supervisor from The University of Hong Kong, Prof. Jiang Li Jun, for his knowledge transfer, references and resources to complete the research of this study. I would also like to thank my colleague from The University of Hong Kong, Mr. Fu Xin, for his good teaching skills and clear explanations on how to use the numerical model (RHESA) that developed by him.

Last but not least, I wish to thank the Asian Office of Aerospace R&D (AOARD) and Malaysia MOSTI Flagship Research Fund for their financial support of this research.

APPROVAL SHEET

This dissertation entitled **"A STUDY OF MICROWAVE REMOTE SENSING OF NATURAL MEDIUM USING RADIATIVE TRANSFER THEORY AND RELAXED HIERARCHICAL EQUIVALENT SOURCE ALGORITHM"** was prepared by LUM CHAN FAI and submitted as partial fulfillment of the requirements for the degree of Master of Engineering Science at Universiti Tunku Abdul Rahman.

Approved by:

____

(Prof. Ir. Dr. EWE HONG TAT) Date: ………………………
Supervisor
Department of Electrical and Electronics Engineering
Lee Kong Chian Faculty of Engineering and Science
Universiti Tunku Abdul Rahman

____

(Mr. LEE YU JEN) Date: ………………………
Co-supervisor
Department of Electronic Engineering
Faculty of Engineering and Green Technology
Universiti Tunku Abdul Rahman

____

(Prof. JIANG LI JUN) Date: ………………………
External co-supervisor
Department of Electrical and Electronic Engineering
Faculty of Engineering
The University of Hong Kong Pokfulam, Hong Kong, China

LEE KONG CHIAN FACULTY OF ENGINEERING AND SCIENCE

UNIVERSITI TUNKU ABDUL RAHMAN

Date:

SUBMISSION OF DISSERTATION

It is hereby certified that **LUM CHAN FAI** (ID No: **14UEM07973**) has completed this dissertation entitled **"A STUDY OF MICROWAVE REMOTE SENSING OF NATURAL MEDIUM USING RADIATIVE TRANSFER THEORY AND RELAXED HIERARCHICAL EQUIVALENT SOURCE ALGORITHM"** under the supervision of Prof. Ir. Dr. Ewe Hong Tat (Supervisor) from the Department of Electrical and Electronics Engineering, Lee Kong Chian Faculty of Engineering and Science, Mr. Lee Yu Jen (Co-Supervisor) from the Department of Electronic Engineering, Faculty of Engineering and Green Technology, and Prof. Jiang Li Jun (External Co-Supervisor) from the Department of Electrical and Electronic Engineering, Faculty of Engineering.

I understand that University will upload softcopy of my dissertation in pdf format into UTAR Institutional Repository, which may be made accessible to UTAR community and public.

Yours truly,

(Lum Chan Fai)

DECLARATION

I (LUM CHAN FAI) hereby declare that the dissertation is based on my original work except for quotations and citations which have been duly acknowledged. I also declare that it has not been previously or concurrently submitted for any other degree at UTAR or other institutions.

Name: Lum Chan Fai
Date: June 2018

TABLE OF CONTENTS

LIST OF TABLES

LIST OF FIGURES

LIST OF ABBREVIATIONS

CEM	Computational electromagnetic
CLPX	Cold land processes field experiment
DDM	Domain decomposition method
DM-PACT	Dense medium phase and amplitude correction theory
DMRT	Dense medium radiative transfer theory
DOY	Day-of-year
EM	Electromagnetic spectrum
EPA	Equivalence principle algorithm
ES	Equivalence surface
ESA	Equivalent source algorithm
FDM	Finite-difference method
FDTDM	Finite-difference time-domain method
FEM	Finite-element method
IEM	Integral equation model
IOP	Intensive observation periods
ISA	Intensive study areas
ISM	Macroscopically isotropic and mirror-symmetric medium
LSOS	Local scale observation site
MLFMA	Multilevel fast multipole algorithm
MoM	Method of Moments
MSA	Meso-cell study areas

PEC	Perfect electric conductor
RHESA	Relaxed hierarchical equivalent source algorithm
RHS	Right hand side
RMS	Root mean square
RT	Radiative transfer
RWG	Rao-Wilton-Glisson
SAR	Synthetic aperture radar
SWE	Snow water equivalent
SWG	Shaubert-Wilton-Glisson
VIE	Volume integral equations

CHAPTER 1

INTRODUCTION

1.1 Research Background

Electromagnetic wave has helped human to interact with the nature in their daily life since the day human exists on earth. The sunlight was an important source of electromagnetic wave that helps human see and observe the earth and this lead to the development of optical remote sensing. Nowadays, this area has extended to microwave remote sensing and other EM spectrum as well.

A lot of phenomena happened on Earth are due to the scattered field observed by our eyes after the electromagnetic wave of sunlight interacts with the objects. Studying how the electromagnetic wave interacts with nature could provide clues and explain why such phenomenon happen on earth. One of the famous and important theories found and awarded the Nobel Prize for Physics in 1904 was proposed by British physicist Lord Rayleigh. The theory called Rayleigh scattering that explains why our sky looks blue. According to Rayleigh scattering, the sky looks blue is because of the scattering of light due to air molecules which sizes are much smaller than the visible light wavelengths. Blue light has the shortest wavelength and is scattered more strongly than long wavelength red light. This explains the phenomenon why the sky looks blue.

Like the eyes of human, active microwave remote sensing is actually a way that uses microwave as a source of electromagnetic wave to monitor the earth terrain through aircraft-based and satellite sensor technologies. Microwave is a spectrum of electromagnetic wave that operates between 300 MHz to 300 GHz frequencies. With such frequencies, it actually can penetrate through the clouds and ground. This allow microwave to detect scatterers embedded inside the mediums. Besides this, the use of microwave to replace the sunlight as a source of illumination allows data collections to be performed either during day or night time.

The scattered field from the earth terrain are captured by the satellite sensor and used to generate microwave images. This information can be interpreted and useful information of earth terrain such as thickness of the sea ice, snow water equivalent (SWE) of terrain and roughness of surfaces can be obtained. This is another reason why remote sensing is getting increasingly important. With remote sensing technology, we can collect data at large scale and over long-term without the need of physically collecting data in dangerous areas. Thus, many countries have active programme to develop and send their satellites to space to monitor the earth terrain or climate change remotely such as RADARSAT, TerraSAR-X or ERS.

Studying the microwave scattering problems and scattering mechanisms through the propagation and radiation of microwave in a medium became popular since World War II. In order to understand better on how microwave actually interacts with a medium, theoretical models were developed to simulate the scattering and radiation of microwave in a medium for the past few decades. Basically, many theoretical models developed based on radiative transfer (RT) theory have been used to study on vegetation and snow or sea ice mediums (Tsang et al., 1985; Ulaby et al., 1986; Tjuatja et al., 1992; Karam et al., 1993; Chuah et al., 1997; Ewe and Chuah, 1998, 1999). The theory is based on the energy transport concept (Chandrasekhar, 1960) that describes the propagation of wave intensity through a medium which is affected by the absorption, emission and scattering in the medium. The radiative transfer equation can be solved by exact solution using eigen-analysis (Shin and Kong, 1989) and matrix doubling method (Leader, 1978; Eom and Fung, 1984; Tjuatja et al., 1992) or by iterative solution (Tsang et al., 1981; Karam et al., 1992). Solving radiative transfer equation iteratively to obtain first and second order solutions can give a better view and details on how scattering mechanisms in the medium are involved.

Generally, theoretical models developed involve the scattering from medium (volume scattering) and the boundaries between the layers (surface scattering). It is important to consider the interactions within the layers (volume-volume scattering) as well as between the layers and the boundaries (surface-volume scattering). A medium is considered as a sparse medium when scatterers are far from each other. When the distance between scatterers is small compared with the wavelength, then the medium is considered as an electrically dense medium.

For the study of a dense medium, several efforts have been done by some previous researchers to improve the modeling of scattering mechanisms by including the phase coherency between scatterers and near-field effect. Dense Medium Radiative Transfer Theory (DMRT) (Tsang and Ishimaru, 1987) and the Dense Medium Phase and Amplitude Correction Theory (DM-PACT) (Chuah et al., 1996, 1997) were two solutions developed to accommodate the dense medium effect. The dense medium radiative transfer theory is based on the quasi-crystalline approximation. For the DM-PACT, the amplitude correction (Fung and Eom, 1985) is included by considering a modified Stokes matrix to take into account the near-field interactions between closely packed scatterers. While for the phase correction (Chuah et al., 1996, 1997) this is to take into account the variance and correlation between scatterers in their random location distribution by adopting the antenna array concept. Following this concept, the scattering phase matrix for a collection of scatterers can be found by multiplying the Stokes matrix of a single scatterer with a phase correction factor. The dense medium phase and amplitude correction theory has been incorporated into the second order radiative transfer iterative solution and applied to different kinds of dense mediums like snow and vegetation (Ewe and Chuah, 1999, 2000).

For surface scattering, several surface models have been developed to calculate the scattering from boundaries between the layers. Kirchhoff model (Fung, 1967; Beckmann and Spizzichino, 1987) is used for very rough surface while small perturbation model (SPM) (Valenzuela, 1967; Fung, 1968) is more suitable for the slightly rough surface. The integral equation method (IEM) (Fung, 1994) is the model known to give good prediction for a wide range of surface roughness. The advanced integral equation method (AIEM) (Chen and Fung, 2003; Wu and Chen, 2004) is the improved model based on IEM.

Traditionally, theoretical models developed normally use some basic shapes of scatterers like sphere, cylinder, disk, ellipsoid or needle to represent the scatterers in the natural mediums. The scattering of these basic shapes can be formulated using analytical solutions. As nowadays computer technologies are much more advanced and provide much faster computational speed, thus solving the complex electromagnetic problem becomes practical and convenient. Computational electromagnetics (CEM) is getting popular and important in the modern engineering field. It is changing the way of solving electromagnetic problems. The emergence of a numerical solution called Method of Moments (MoM) has brought the next height of CEM as it transforms the integral equations into a linear system that a computer can solve it approximately. Thus, incorporation of the existing RT theoretical model with CEM would be a right direction to move on.

1.2 Problem Statement

From the past research works, the radiative transfer theory has been applied to two of the existing scattering models that applied to snow or sea ice and vegetation mediums. These RT theoretical models can simulate the total backscattering for a single layer or multiple layers of a medium. Traditionally, these RT theoretical models are developed based on analytical solution and some basic shapes are used to represent the scatterers inside the medium. Generally, the theoretical model used to simulate the snow or sea ice medium is assumed the scatterers are spherical while for the vegetation medium, scatterers are assumed in some basic shapes like cylinder, disk or ellipsoid.

To further extend the existing RT theoretical models to help better understand the microwave interacts with different kinds of shapes of scatterers inside a medium, we need to integrate the existing RT theoretical models with numerical solutions like equivalence principle algorithm (EPA) and relaxed hierarchical equivalent source algorithm (RHESA). Using these numerical solutions, the new improved RT theoretical models can simulate different kinds of shapes of scatterers without the need of formula derivation for every newly added shape. This allows the new theoretical model to be applied to different kind of media where scatterers are irregular shape.

1.3 Objectives

The objectives of this research are as follow:

i. To determine the suitability of computational electromagnetics in solving electromagnetic scattering problems faced in remote sensing field.
ii. To develop an improved RT theoretical model that will be based on computational electromagnetics for remote sensing of random discrete medium such as snow layer with irregular shape of scatterers.
iii. To better understand how scattering of different shape of scatterers interact with microwave through new improved RT theoretical model.
iv. To validate the new improved RT theoretical model and analyze its performance with recent ground truth measurements of earth terrain and satellite data.

1.4 Dissertation Outline

There are total eight chapters in this dissertation. The first chapter is about research background about remote sensing, theoretical models, solutions and theories developed by previous researchers. The chapter also includes the objectives of this research work and some basic survey on the current trend in solving scattering problems. Chapter Two is about literature review of existing RT theoretical model based on intensity approach that adopts the radiative transfer theory which adopted the dense medium phase and amplitude correction theory. This chapter also discusses the limitation of existing RT theoretical model faced and what can be done to improve further and extend the use of current RT theoretical model. Recent trend in computational electromagnetics (CEM) and method of moments (MoM) are also discussed. Chapter Three is about the development of a theoretical model that incorporates the equivalence principle algorithm (EPA) with detailed formulation. Chapter Four is about the theoretical analysis done using the theoretical model base on RT that incorporates EPA (RT-EPA model). Chapter Five is about the development of a theoretical model that incorporates the relaxed hierarchical equivalent source algorithm (RHESA) by eliminating the constraints faced by the RT-EPA model. Chapter Six is about the theoretical analysis done using the theoretical model that incorporates RHESA (RT-RHESA model). Chapter Seven is about the application of the improved RT theoretical model (RT-RHESA model) to compare the simulated results with ground truth measurement and satellite data. Chapter Eight is about the summary and conclusion of this study, limitation of the new RT-RHESA model and suggestions for future improvements.

CHAPTER 2

LITERATURE REVIEW

2.1 Existing Radiative Transfer (RT) Theoretical Model

There were scattering models developed based on radiative transfer theory which have been applied on two major types of mediums which are snow or sea ice (Tjuatja et al., 1992; Du et al., 2005; Lee et al., 2011; Albert et al., 2012; Syahali and Ewe, 2013) and vegetation (Eom and Fung, 1984; Karam et al., 1992, 1993; Ewe and Chuah, 1999, 2000). Theoretical models were developed to help understand how microwave interacts with a natural medium. Both single layer and multiple layers of scattering models were developed from the past (Tjuatja et al., 1992; Tzeng et al., 1992; Chuah et al., 1997; Ewe and Chuah, 1999; 2000; Albert et al., 2012). The forward model was used to simulate and obtain the backscattering coefficient which can then be compared with data from satellite (SAR) images. With the predictions of backscattering coefficient from the forward model, inverse model can be developed to estimate and retrieve some of the useful parameters such as snow thickness (Lee et al., 2011) or estimate the snow water equivalent (SWE) (Besic et al., 2012).

For the study of this research, we would focus on scattering problems for a layer of snow where integration of this model with CEM solution will be pursued. The RT theoretical model was developed based on intensity approach that adopts the radiative transfer theory. With this, through energy transport concept (Chandrasekhar, 1960), we can describe the propagation of wave intensity in a medium by considering the absorption, emission and scattering in the medium. For a dense medium like snow, the scatterers are closely packed, the existing RT theoretical model includes the dense medium phase and amplitude correction theory (DM-PACT) (Chuah et al., 1996, 1997) to study it. The theory has taken into account the near-field interactions between scatterers by applying a modified phase matrix which takes in the near-field term of the scattered field of the scatterers and coherent effect of the scatterers by multiplying Stokes matrix of a single scatterer with a phase correction factor. Besides this, the RT theoretical model has included the integral equation model (IEM) (Fung et al., 1997; Fung and Chen, 2004; Wu and Chen, 2004) to calculate the surface scattering from the top and bottom surfaces. The iterative formulation of radiative transfer equation was solved up to second order solution (Ewe and Chuah, 1998, 1999). Three major scattering mechanisms have been considered in the current RT theoretical model and they consist of surface scattering, surface-volume scattering and volume scattering. Traditionally, ice particles inside a snow layer were assumed in spherical shape. Scattering from these spherical scatterers was calculated using Mie-scattering formulation. The use of Mie phase matrix was included in scattering model with amplitude correction by (Fung and Eom, 1985). Later the method was further used by (Tjuatja et al., 1992) in the development of scattering model using matrix doubling method for snow-covered sea ice. The phase array correction solution was added in by Chuah et al. (1996, 1997) to take into account for coherency effect of the scatterers. Although the matrix doubling method provides a full solution of the multiple scattering problem and gives satisfactory predictions compared to measurement data, further investigation of scattering mechanisms behind the propagation of wave intensity through a medium was later performed by Ewe and Chuah (1998, 1999) using iterative solution of the radiative transfer equation that was solved up to second order scattering.

The scattering model developed based on second order radiative transfer equation was used for vegetation medium as well (Ewe and Chuah, 1999, 2000). Basic shapes like cylinder, disk, ellipsoid or needle were used to represent the leaves, branches and trunks of vegetation. To calculate the scattered fields from disk, ellipsoid and needle-shaped scatterers, Rayleigh-Gans approximation was used (Van De Hulst, 1981). The needle and disk-shaped scatterers were approximated by using thin oblate spheroids and long prolate spheroids. While for cylindrical scatterers, infinitely long circular cylinder was first studied and resolved by Rayleigh (Wait, 1955; Ruck et al., 2002), and the oblique incidence case was later discussed by Wait (1955, 1959). In 1988, Karam and Fung (1988) adapted the scattering solution of the infinitely long cylinder to cylinder with finite length. The scattered field derivation for a finite length dielectric cylinder was calculated through the infinite cylinder approximation. This means that the scattered field obtained from those shape of scatterers in the scattering model of vegetation were approximated. The scattered fields from cylinder, disk, ellipsoid or needle were derived analytically.

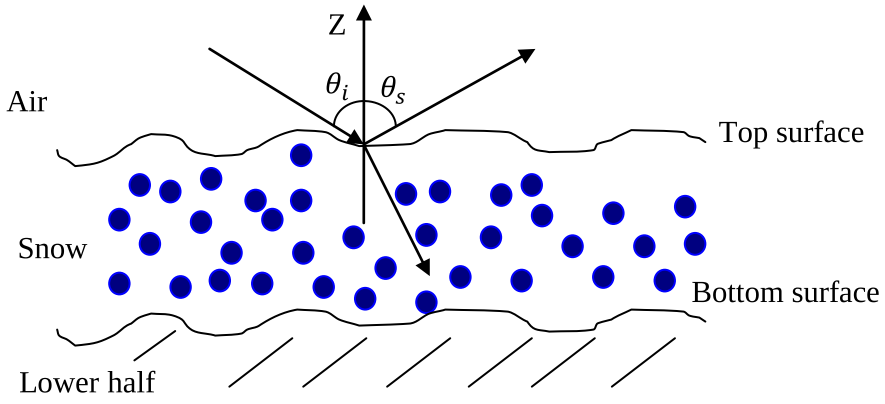

Figure 2.1 Illustration of model configuration for a layer of snow with spherical scatterers.

Figure 2.1 shows the model configuration of a layer of snow with spherical scatterers embedded inside. In the modeling configuration, there are three layers which consist of air layer as top layer, snow layer as middle (background) layer and the soil, water or sea ice to be the lower half layer. The boundary between the air layer and snow layer becomes the top rough surface and the boundary between snow layer and soil, water or sea ice layer becomes the rough bottom surface. Generally, to calculate a layer of snow using existing RT theoretical model there are several parameters that are needed to be configured such as incidence angle, frequency of incidence wave, radius size of scatterer, relative permittivity of scatterer, volume fraction of scatterers, relative permittivity of top, middle and bottom mediums, thickness of snow layer, root mean square (RMS) height of top surface, correlation length of top surface, root mean square (RMS) height of bottom surface and correlation length of bottom surface.

2.2 Formulation of Mie-scattering Model

The radiative transfer theory characterizes the propagation and scattering of specific wave intensity inside a medium and it is written in Equation 2.1 (Fung, 1994):

$$\cos\theta \frac{d\bar{I}}{dz} = -\bar{\bar{K}}_e \bar{I} + \int \bar{\bar{P}} \bar{I} d\Omega \tag{2.1}$$

where $\bar{I}$, $\bar{\bar{P}}$, and $\bar{\bar{K}}_e$ are the Stokes vector, phase matrix and extinction matrix of the medium. The modified Stokes parameters is used to relate the electric field of an elliptically polarized plane wave, $\bar{E} = (E_v\hat{v} + E_h\hat{h})e^{-j\bar{k}\bar{r}}$, to the four components of Stokes vector as written in Equation 2.2:

$$\bar{I} = \begin{bmatrix} I_v d\Omega \\ I_h d\Omega \\ U d\Omega \\ V d\Omega \end{bmatrix} = \begin{bmatrix} \dfrac{\langle |E_v|^2 \rangle}{\eta} \\ \dfrac{\langle |E_h|^2 \rangle}{\eta} \\ \dfrac{2}{\eta} Re\langle E_v E_h^* \rangle \\ \dfrac{2}{\eta} Im\langle E_v E_h^* \rangle \end{bmatrix} \tag{2.2}$$

where I_v is the vertically polarized specific intensity, I_h is the horizontally polarized specific intensity, U and V represent the correlations between the vertically and horizontally polarizations, as shown in Equation 2.2 respectively. $d\Omega$ is the differential solid angle that the wave propagating through and η is the intrinsic impedance of the medium. In Mie-scattering model, due to the spherical symmetry, Equation 2.2 can be simplified only to consider the first two components of Stokes vector which are I_v and I_h. The phase matrix $\overline{\overline{P}}$ for the first two elements of Stokes parameters of a collection of scatterers is a 2 × 2 matrix which consists of Stokes matrix of a single scatterer multiplied with a phase correction factor of a unit volume of scatterers. The formulation of the phase matrix is written in Equation 2.3:

$$\overline{\overline{P}}\left(\theta,\, \emptyset;\, \theta',\, \emptyset'\right) = \langle|\Psi|^2\rangle_n \cdot \overline{\overline{S}} = \langle|\Psi|^2\rangle_n \cdot \begin{bmatrix} S_{vv} & S_{vh} \\ S_{hv} & S_{hh} \end{bmatrix} = \begin{bmatrix} P_{vv} & P_{vh} \\ P_{hv} & P_{hh} \end{bmatrix} \tag{2.3}$$

where $\overline{\overline{S}}$ is the Stokes matrix for a Mie-scatterer with the close spacing amplitude correction and $\langle|\Psi|^2\rangle_n$ is the dense medium phase correction factor (Chuah et al., 1996). The full expression of 4 × 4 phase matrix $\overline{\overline{P}}$ is listed in APPENDIX A. The phase matrix $\overline{\overline{P}}$ is a matrix that connects the Stokes parameters of the incidence and scattered beams in a random medium. The single scatterer's Stokes matrix $\overline{\overline{S}}$ is given in the following expression by Tjuatja et al. (1992) and Chuah et al. (1997)

$$\overline{\overline{S}} = \frac{d^2\eta}{|E_o|^2} Re \begin{bmatrix} (E_v^s H_h^{s*})_{v\text{-}inc} & (E_v^s H_h^{s*})_{h\text{-}inc} \\ -(E_h^s H_v^{s*})_{v\text{-}inc} & -(E_h^s H_v^{s*})_{h\text{-}inc} \end{bmatrix} \qquad (2.4)$$

where d is the average distance between scatterers which has the following expression:

$$d = (v_o/v_f)^{1/3} \qquad (2.5)$$

where v_o is the volume of scatterer which in this case is sphere thus $v_o = \frac{4}{3}\pi a^3$ and v_f is the volume fraction of scatterers per unit volume. The extinction matrix $\overline{\overline{K}}_e$ includes the absorption loss from the background medium and the scatterers ($\overline{\overline{K}}_a$) as well as the scattering loss from the scatterers ($\overline{\overline{K}}_s$).

To solve Equation 2.1, we first have to find the extinction coefficient $\overline{\overline{K}}_e$ and phase matrix $\overline{\overline{P}}$. The extinction matrix $\overline{\overline{K}}_e$ is the total sum of scattering coefficient $\overline{\overline{K}}_s$ and absorption coefficient $\overline{\overline{K}}_a$. The formula is written in Equation 2.6:

Volume extinction coefficient

$$\overline{\overline{K}}_e = \overline{\overline{K}}_s + \overline{\overline{K}}_a \qquad (2.6)$$

where the scattering coefficient $\overline{\overline{K}}_s$ can be derived by the total scattered power from a scatterer multiplied by the number of scatterers per unit volume (n_o)

$$\bar{\bar{K}}_{sp}(\theta_i,\phi_i) = n_o \int_0^{2\pi} \int_0^{\pi} (S_{vp}+S_{hp}) \sin\theta_s \, d\theta_s d\phi_s \tag{2.7}$$

where p is polarization and S is respective component of Stokes matrix. For uniformly distributed, and homogenous spherical scatterers, the above scattering coefficient is independent of incidence direction, thus $\bar{\bar{K}}_{sv}$ and $\bar{\bar{K}}_{sh}$ are the same.

For absorption coefficient $\bar{\bar{K}}_a$ for p polarization it is given by Fung (1994) as

$$\bar{\bar{K}}_{ap} = 2k_o \left| Im\sqrt{\varepsilon_{ap}} \right| \tag{2.8}$$

where k_o is the wavenumber in free space, ε_{ap} is the effective relative permittivity of the medium. Like the scattering coefficient, the absorption and extinction coefficients are also independent of the incidence direction.

To calculate the scattered field from the sphere analytically using Mie-scattering formulation, we can consider an incidence wave propagating in $+\hat{z}$ direction toward a sphere with relative permittivity $\varepsilon_r = \varepsilon' - j\varepsilon''$ and radius a as shown in Figure 2.2. The permeability μ of the sphere and background medium are the same. The electric and magnetic fields (with time dependence expression of $e^{j\omega t}$ suppressed) are given by

$$\overline{E}^i = \hat{x}E_o e^{-jkz} \tag{2.9}$$

$$\overline{H}^i = \hat{y}\frac{E_o}{\eta}e^{-jkz} \tag{2.10}$$

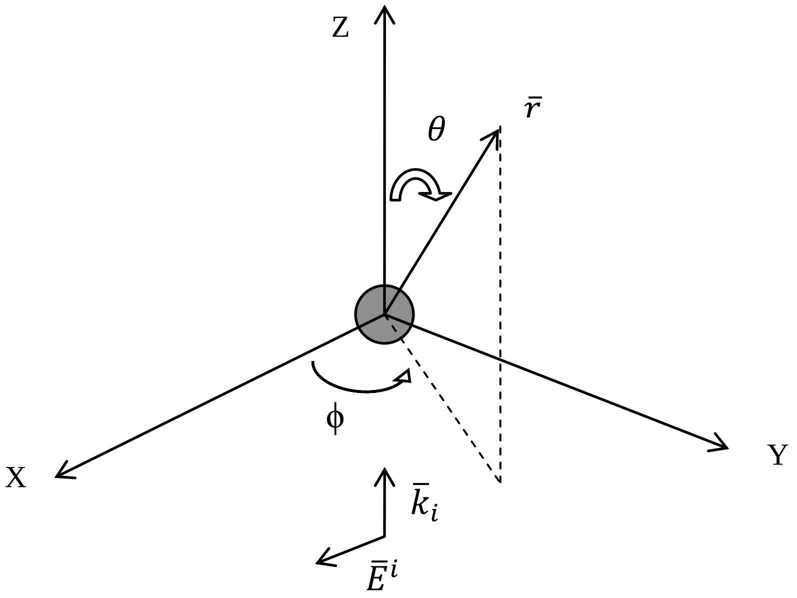

Figure 2.2 Scattering geometry for a single sphere and incidence wave.

where $k = \omega\sqrt{\mu\varepsilon}$ and $\eta = \sqrt{\mu/\varepsilon}$.

The scattered fields due to the sphere are then given by Van de Hulst (1981) as

$$\overline{E}^s = E_o\sum_{n=1}^{\infty}(-j)^n\frac{(2n+1)}{n(n+1)}\left\{-b_n\overline{m}^{(3)}_{o1n}-ja_n\overline{n}^{(3)}_{e1n}\right\} \tag{2.11}$$

$$\overline{H}^s = \frac{E_o}{\eta}\sum_{n=1}^{\infty}(-j)^n\frac{(2n+1)}{n(n+1)}\left\{a_n\overline{m}^{(3)}_{e1n}-jb_n\overline{n}^{(3)}_{o1n}\right\} \tag{2.12}$$

where a_n and b_n are the Mie coefficients given by Fung (1994)

$$a_n = \frac{\sqrt{\varepsilon_r}\hat{J}_n'(u)\hat{J}_n(v)-\hat{J}_n(u)\hat{J}_n'(v)}{\sqrt{\varepsilon_r}\left[\hat{H}_n^{(2)}(u)\right]'\hat{J}_n(v)-\hat{H}_n^{(2)}(u)\hat{J}_n'(v)} \tag{2.13}$$

$$b_n = \frac{\sqrt{\varepsilon_r}\hat{J}_n(u)\hat{J}_n'(v)-\hat{J}_n'(u)\hat{J}_n(v)}{\sqrt{\varepsilon_r}\left[\hat{H}_n^{(2)}(u)\right]\hat{J}_n'(v)-\left[\hat{H}_n^{(2)}(u)\right]'\hat{J}_n(v)} \tag{2.14}$$

where $u = ka$, $v = k\sqrt{\varepsilon_r}a = k_s a$. $\hat{J}_n(\varphi)$ is the Ricatti-Bessel function and $\hat{H}_n^{(2)}(\varphi)$ is the Ricatti-Hankel function of the second kind, and $\varphi = u,v$. $[\ ]'$ denotes differentiation with respect to the argument. The spherical vector wave function $\overline{m}^{(3)}_{o1n}$ and $\overline{n}^{(3)}_{e1n}$ with subscripts o and e denote odd and even can be expressed by the spherical Hankel function of the second kind $h_n^{(2)}(kr)$, and the associated Legendre polynomials $P_n^1(\cos\theta)$. The expressions are given by Fung (1994) as:

$$\overline{m}^{(3)}_{\substack{o\\e}1n} = \pm\hat{\theta}\frac{1}{\sin\theta}h_n^{(2)}(kr)P_n^1(\cos\theta)\begin{matrix}\cos\phi\\ \sin\phi\end{matrix} - \hat{\phi}h_n^{(2)}(kr)\frac{\partial}{\partial\theta}\left\{P_n^1(\cos\theta)\right\}\begin{matrix}\sin\phi\\ \cos\phi\end{matrix} \tag{2.15}$$

$$\overline{n}_{\substack{o\\e}1n}^{(3)} = \hat{r}\frac{n(n+1)}{kr}h_n^{(2)}(kr)P_n^1(\cos\theta)\begin{matrix}\sin\phi\\\cos\phi\end{matrix}+$$

$$\hat{\theta}\frac{1}{kr}\frac{dy}{d(kr)}\left\{krh_n^{(2)}(kr)\right\}\frac{\partial}{\partial\theta}\left\{P_n^1(\cos\theta)\right\}\begin{matrix}\sin\phi\\\cos\phi\end{matrix}\pm$$

$$\hat{\phi}\frac{1}{kr\sin\theta}\frac{d}{d(kr)}\left\{krh_n^{(2)}(kr)\right\}P_n^1(\cos\theta)\begin{matrix}\cos\phi\\\sin\phi\end{matrix} \tag{2.16}$$

where *r* is the range where scattered fields are measured.

In order to support arbitrary incidence angles and different polarizations, the scattered fields in Equations 2.11 and 2.12 can be converted into vertically or horizontally polarized incidence wave through a coordinate transformation. Detailed explanations of the transformation has been given in (Fung, 1994) and (Fung and Eom, 1985).

After solving the integro-differential expression in Equation 2.1 iteratively up to second order, the bistatic scattering coefficient which relates the scattered intensities to the incidence intensities with incidence wave polarization *q* and scattered wave polarization *p* can be obtained as:

$$\sigma_{pq}\left(\theta_s,\phi_s,\theta_i,\phi_i\right) = \sigma_{pq}(0)+\sigma_{pq}(1)+\sigma_{pq}(2) \tag{2.17}$$

Equation 2.17 consists of solutions of Equation 2.1 with different order where the value inside the bracket indicates the order of solutions which are zeroth, first and second order, respectively. *p* and *q* are the polarizations of incidence and scattered fields. (θ_s,ϕ_s) and (θ_i,ϕ_i) are the scattered angles and incidence angles, respectively.

Detailed contribution terms of $\sigma_{pq}(0)$, $\sigma_{pq}(1)$, and $\sigma_{pq}(2)$ are given by Fung (1994) as:

$$\sigma_{pq}(0) = \sigma_{pq}^{s} = \sigma_{pq}^{s1} + \sigma_{pq}^{s2} \tag{2.18}$$

$$\sigma_{pq}(1) = \sigma_{pq}^{vs}(m \rightarrow s2) + \sigma_{pq}^{vs}(s2 \rightarrow m) + \sigma_{pq}^{v}(up,down) \tag{2.19}$$

$$\sigma_{pq}(2) = \sigma_{pq}^{v}(up,up,down) + \sigma_{pq}^{v}(up,down,down) \tag{2.20}$$

where the superscript s is the surface scattering terms, vs is the surface-volume scattering terms and v is the volume scattering terms. The top and bottom surfaces are denoted by superscripts s1 and s2, respectively. For surface-volume scattering terms vs it can have the volume to bottom surface scattering terms $(m \rightarrow s2)$ and the bottom surface to volume scattering terms $(s2 \rightarrow m)$. For volume scattering terms v it can have the direct volume scattering terms $(up,down)$ and double volume scattering terms which are $(up,up,down)$ and $(up,down,down)$. Further explanations of all scattering terms mentioned above can be found in Section 2.2.1.

Given the Equations 2.18, 2.19 and 2.20 above, the bistatic scattering coefficient in Equation 2.17 can then be rewritten as:

$$\sigma_{pq}\left(\theta_s,\phi_s,\theta_i,\phi_i\right) = \sigma^{s}_{pq} + \sigma^{vs}_{pq} + \sigma^{v}_{pq} \tag{2.21}$$

2.2.1 Surface Scattering Terms

The contribution from surface consists of scattering from the top and bottom surfaces of a random medium as shown in Figure 2.3. IEM model was used with existing RT theoretical model to calculate the scattering from these surfaces.

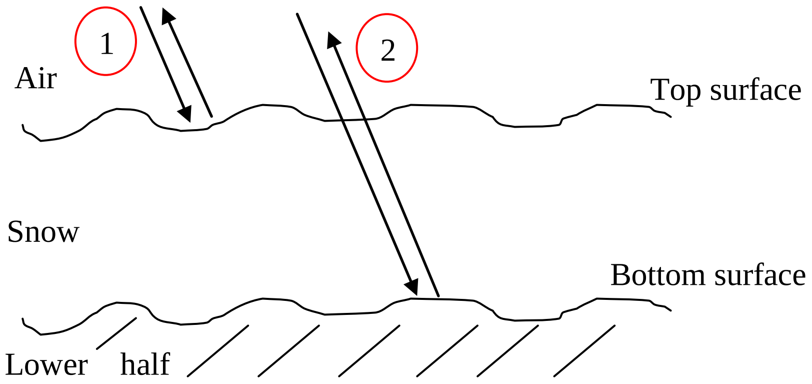

Figure 2.3 Illustration of top surface scattering (1) and bottom surface scattering (2).

The bistatic single-scatter scattering coefficient expressions for the top surface σ^{s1}_{pq} and the bottom surface σ^{s2}_{pq} are given by Ewe and Chuah (1998) as:

$$\sigma^{s1}_{pq}(\theta_s,\phi_s,\theta_i,\phi_i) = \sigma^{o1}_{pq}(\theta_s,\phi_s,\theta_i,\phi_i) \tag{2.22}$$

$$\sigma_{pq}^{s2}\left(\theta_s,\phi_s,\theta_i,\phi_i\right) = \cos\theta_s\, T_{1tp}(\theta_s,\theta_{ts})T_{t1q}(\theta_{ti},\theta_i)\cdot$$

$$\sec\theta_{ts}\, L_p(\theta_{ts})L_q(\theta_{ti})\sigma_{pq}^{o2}(\theta_{ts},\phi_{ts},\theta_{ti},\phi_{ti}) \tag{2.23}$$

where σ_{pq}^{o1} and σ_{pq}^{o2} are the bistatic scattering coefficient of top surface and bottom surface based on IEM rough surface model, respectively. θ_i and θ_s are the incidence and scattered polar angle in the air. θ_{ti} and θ_{ts} are the incidence and scattered polar angle in a random layer and are related to the incidence and scattered polar angle in the air through the Snell's Law. There are also transmissivity from top boundary into the layer $T_{t1q}(\theta_{ti},\theta_i)$ and from layer into the top boundary $T_{1tp}(\theta_s,\theta_{ts})$. $L_p(\theta_{ts})$ and $L_q(\theta_{ti})$ are the attenuation through the layer and are given as:

$$L_u(\theta) = \exp[-K_{eu}(\theta)d_l \sec\theta] \tag{2.24}$$

where $u = p, q$, d_l is the layer thickness and K_{eu} is the volume extinction coefficient.

2.2.2 Surface-Volume Scattering Terms

As shown in Figure 2.4, the contribution from surface-volume consists of scattering from volume to bottom surface and bottom surface to volume.

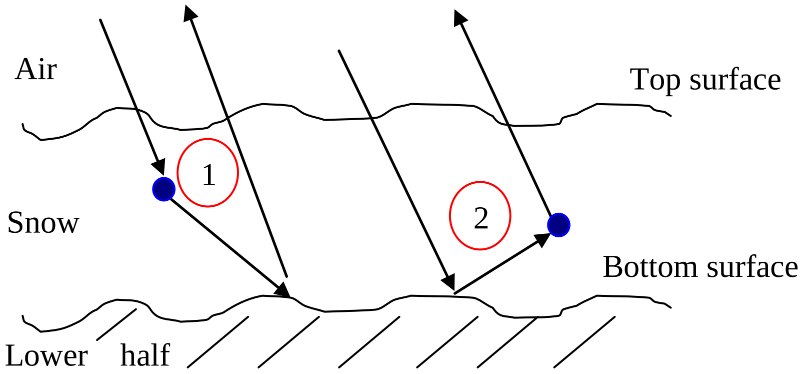

Figure 2.4 Illustration of volume to bottom surface scattering (1) and bottom surface to volume scattering (2).

The formulations for the first order surface-volume scattering terms which involve the scattering from volume to bottom surface and bottom surface to volume are given as:

$$\sigma_{pq}^{vs}(m \rightarrow s2) = \cos\theta_s \, T_{1tp}(\theta_s,\theta_{ts}) T_{t1q}(\theta_{ti},\theta_i) L_p(\theta_{ts}) \sec\theta_{ts}$$

$$\int_0^{2\pi} d\phi \int_0^{\frac{\pi}{2}} \sin\theta \sec\theta \, d\theta \sum_{u=v,h} \sigma_{pu}^{s2}\left(\theta_{ts},\phi_{ts};\pi\text{-}\theta,\phi\right) P_{uq}\left(\pi\text{-}\theta,\phi;\pi\text{-}\theta_{ti},\phi_{ti}\right)$$

$$\frac{L_u(\theta)\text{-}L_q(\theta_{ti})}{K_{eq}(\theta_{ti})\sec\theta_{ti}\text{-}K_{eu}(\theta)\sec\theta} \qquad (2.25)$$

$$\sigma_{pq}^{vs}(s2 \rightarrow m) = \cos\theta_s \, T_{1tp}(\theta_s,\theta_{ts}) T_{t1q}(\theta_{ti},\theta_i) L_q(\theta_{ti}) \sec\theta_{ts}$$

$$\int_0^{2\pi} d\phi \int_0^{\frac{\pi}{2}} \sin\theta \sec\theta \, d\theta \sum_{u=v,h} P_{pu}\left(\theta_{ts},\phi_{ts};\theta,\phi\right) \sigma_{uq}^{s2}\left(\theta,\phi;\pi\text{-}\theta_{ti},\phi_{ti}\right)$$

$$\frac{L_p(\theta_{ts})\text{-}L_u(\theta)}{K_{eu}(\theta)\sec\theta\text{-}K_{ep}(\theta_{ts})\sec\theta_{ts}} \qquad (2.26)$$

where P_{pu} is the phase matrix for a collection of scatterers and σ_{uq}^{s2} is the scattering from bottom surface.

2.2.3 Volume Scattering Terms

There are three volume scattering terms as shown in Figure 2.5 which consist of one first order solution for direct volume scattering and two second order solutions for volume-volume scattering terms of which incidence wave is scattered following either the down-down-up or down-up-up sequences.

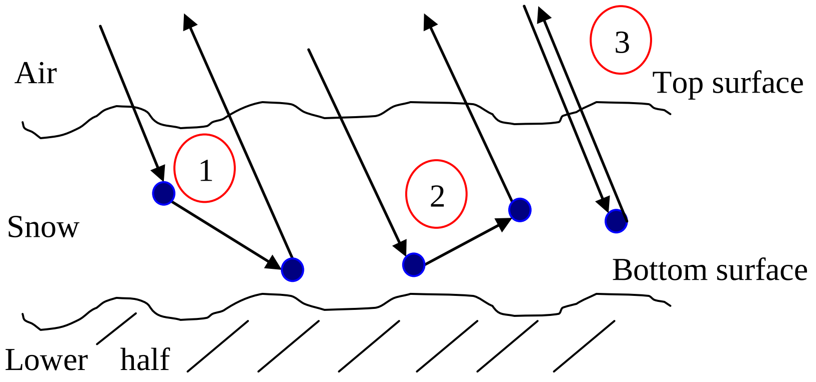

Figure 2.5 Illustration of down-down-up (1) volume-volume scattering, down-up-up volume-volume scattering (2) and direct volume scattering (3).

The formulations for the first order solution for direct volume scattering terms and the second order solution for volume-volume scattering terms of which incidence wave is scattered following the down-down-up and down-up-up sequences are given as:

$$\sigma_{pq}^{v}(up,down) = 4\pi \cos\theta_s\, T_{1tp}(\theta_s,\theta_{ts}) T_{t1q}(\theta_{ti},\theta_i) \sec\theta_{ts}$$

$$P_{pq}\left(\theta_{ts},\phi_{ts};\pi\text{-}\theta_{ti},\phi_{ti}\right) \frac{1\text{-}L_p(\theta_{ts})L_q(\theta_{ti})}{K_{ep}(\theta_{ts}) \sec\theta_{ts} + K_{eq}(\theta_{ti}) \sec\theta_{ti}} \tag{2.27}$$

$$\sigma_{pq}^{v}(up,up,down) = 4\pi \cos\theta_s\, T_{1tp}(\theta_s,\theta_{ts}) T_{t1q}(\theta_{ti},\theta_i) \sec\theta_{ts}$$

$$\int_0^{2\pi} d\phi \int_0^{\frac{\pi}{2}} \sin\theta \sec\theta\, d\theta \sum_{u=v,h} \left\{ \frac{P_{pu}\left(\theta_{ts},\phi_{ts};\theta,\phi\right) P_{uq}\left(\theta,\phi;\pi\text{-}\theta_{ti},\phi_{ti}\right)}{K_{eq}(\theta_{ti}) \sec\theta_{ti} + K_{eu}(\theta) \sec\theta} \right.$$

$$\left. \left[\frac{1\text{-}L_p(\theta_{ts})L_q(\theta_{ti})}{K_{ep}(\theta_{ts}) \sec\theta_{ts} + K_{eq}(\theta_{ti}) \sec\theta_{ti}} + \frac{L_q(\theta_{ti})\left[L_u(\theta)\text{-}L_p(\theta_{ts})\right]}{K_{eu}(\theta) \sec\theta \text{-} K_{ep}(\theta_{ts}) \sec\theta_{ts}} \right] \right\} \tag{2.28}$$

$$\sigma_{pq}^{v}(up,down,down) = 4\pi \cos\theta_s\, T_{1tp}(\theta_s,\theta_{ts}) T_{t1q}(\theta_{ti},\theta_i) \sec\theta_{ts}$$

$$\int_0^{2\pi} d\phi \int_0^{\frac{\pi}{2}} \sin\theta \sec\theta\, d\theta \sum_{u=v,h} \left\{ \frac{P_{pu}\left(\theta_{ts},\phi_{ts};\pi\text{-}\theta,\phi\right) P_{uq}\left(\pi\text{-}\theta,\phi;\pi\text{-}\theta_{ti},\phi_{ti}\right)}{K_{ep}(\theta_{ts}) \sec\theta_{ts} + K_{eu}(\theta) \sec\theta} \right.$$

$$\left. \left[\frac{1\text{-}L_p(\theta_{ts})L_q(\theta_{ti})}{K_{ep}(\theta_{ts}) \sec\theta_{ts} + K_{eq}(\theta_{ti}) \sec\theta_{ti}} + \frac{L_p(\theta_{ts})\left[L_u(\theta)\text{-}L_q(\theta_{ti})\right]}{K_{eu}(\theta) \sec\theta \text{-} K_{eq}(\theta_{ti}) \sec\theta_{ti}} \right] \right\} \tag{2.29}$$

where (*up,down*), (*up,down,down*) and (*up,up,down*) indicate the incidence wave scattering sequences. For (*up,down,down*) sequence as shown in Figure 2.5 red circle 1, it shows that the incidence wave is first scattered downward by a scatterer and then the wave is scattered upward by a second scatterer toward the observation point. For (*up,up,down*) sequence as shown in Figure 2.5 red circle 2, it shows that the incidence wave is first scattered upward by a scatterer then the wave is further scattered upward by another scatterer toward the observation point. Finally, for (*up,down*) sequence as shown in Figure 2.5 red circle 3, it shows that the incidence wave is scattered upward by a scatterer toward the observation point.

2.3 Limitation of Existing Radiative Transfer (RT) Theoretical Model

The existing RT theoretical model with the Mie-scattering solution is only capable of simulating scatterers that are in spherical shape. When it comes to theoretical model for the simulation of snow or sea ice layer, the ice particles or brine inclusions are traditionally assumed in spherical shape. Although existing RT theoretical model is able to give reasonable prediction that agrees well with some ground truth measurement data (Albert et al., 2012) but there are still much room for improvement as in nature there are various types of media such as clouds, raindrops, aerosols, different ice types like river ice, frazil ice and snow ice (Rees, 2005; Gherboudj et al., 2007) where the scatterers inside these kinds of media are normally non-spherical shape.

The shape of ice particles may vary as weather changes or time passes. The snow metamorphism process is a process that describes the change of physical structure of ice particles that happen due to change in temperature or pressure. Further explanation and detail about snow metamorphism can be found in (Colbeck, 1982).

Besides this, there are other previous studies and research works also show that the shape of scatterers can be in granular or tubular form for different types of ice (Gherboudj et al., 2007). The sintering process is a process that describes how ice particles are joined together by bonds (Colbeck, 1997). The form of the new bonded grains can be very different from spherical shape that is normally used in existing RT theoretical model.

In Figure 2.6, it shows some of the shapes of snow samples which are found in the real world by Colbeck (1982) and Tsang et al. (2013).

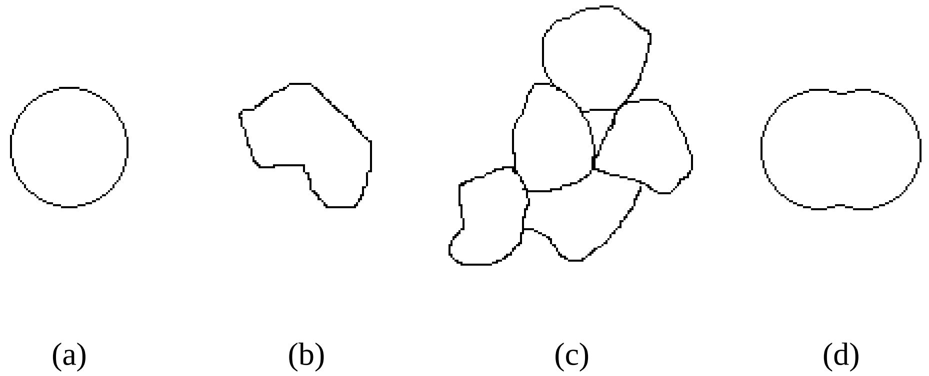

Figure 2.6 Shapes of snow samples (a) sphere, (b) facets, (c) melt-refreeze aggregate and (d) peanut.

From the past research works, to simulate a layer of snow with radiative transfer equation, spherical shape was selected due to its simple form of shape and easy formulations of scattered field where it can be derived analytically. During that time computer was not common and computer technologies are not as advanced as now. This has limited the existing RT theoretical model to be used in different kind of media where scatterers are not in spherical shape. In order to simulate non-spherical shape of scatterers, new formations have to be derived analytically each time when there is new shape to be added to the scattering model. Derive new formulations can be time-consuming and difficult to achieve especially when the shape is far more complex and random.

In addition to that, new formulations have to be derived whenever a new shape needs to be added to existing RT theoretical model, this also involves a lot of codes modification or even development of new programs in order to simulate just one new shape using the scattering model. Major code modifications can be time consuming and when there are enough additional shapes added to the scattering model (especially to model natural earth terrain realistically), code maintenances of the scattering model can be difficult.

2.4 Numerical Solutions

To better understand how microwave interacts with a medium where embedded scatterers are irregular shape, research on how the shape of scatterers could affect the simulated total backscattering coefficient is needed, thus developing a new improved RT theoretical model which can better represent the real shape of scatterers by using numerical solution can fit the task. Numerical solution can help in this when modeling of irregular shape of scatterers is involved.

Computational electromagnetics (CEM) is gaining importance in modern engineering (Chenga Lu and Chew, 1995; Lu and Shen, 1997; Li and Chew, 2007; Fu et al., 2016a; Li et al., 2017). As nowadays computer is getting more powerful and faster in computation, integration existing RT theoretical model with CEM will enable the RT theoretical model to have the ability to simulate irregular shape of scatterers.

In CEM, one of the important roles is its geometrical characterizations of random medium. With this, scatterers to be simulated are modeled in 3D geometry forms and are well defined. A better structure that represents the real scatterer form can provide a possible way on understanding how different shape of scatterers could contribute to total backscattering coefficient and this also can be extended to the current RT theoretical model to be used for different kind of earth media.

2.4.1 Computational Electromagnetics Algorithms

Many CEM methods have been invented and used widely, such as multilevel fast multipole algorithm (MLFMA) (Lu and Chew, 1994), finite-difference method (FDM) (Lu and Shen, 1997), finite-difference time-domain method (FDTDM) (Taflove and Hagness, 2005), equivalence principle algorithm (EPA) (Li and Chew, 2007), finite-element method (FEM) (Jin, 2015) and relaxed hierarchical equivalent source algorithm (RHESA) (Fu et al., 2016a).

Generally, the above mentioned CEM methods can be categorized into two major categories. One is the differential equation method and another one is the integral equation method.

- **Differential Equation Methods**
    - Finite-difference time-domain method (FDTDM)
    - Finite-element method (FEM)
    - Finite-difference method (FDM)
- **Integral Equation Methods**
    - Multilevel fast multipole algorithm (MLFMA)
    - Equivalence principle algorithm (EPA)
    - Relaxed hierarchical equivalent source algorithm (RHESA)

To solve the electromagnetic problems with computer, the integro-differential equations have to be converted into a linear system of equations that a computer can solve it approximately. The following section will further discuss on how this can be performed by using a widely used and famous numerical technique.

2.4.2 Method of Moments (MoM)

The method of moments (MoM) is a widely and famous numerical technique used to convert an integro-differential into matrix form linear equations. MoM was first introduced by Harrington (1987) and applied to field computation problems. Since then, MoM became the mainstay in the computation of electromagnetic problems.

In electromagnetic problems, computing the unknown charge or current distributed on the scatterer is the key solution for integro-differential equations. Generally, a linear integro-differential equation has the form as follows (Harrington, 1987; Gibson, 2007):

$$L(f) = g \tag{2.30}$$

where L is a linear integro-differential operator, f is unknown charge or current and g is a known excitation source (incidence field). The unknown charge f can be expanded in a series of sum of N weighted basis functions (Gibson, 2007):

$$f = \sum_{n=1}^{N} a_n f_n \tag{2.31}$$

where a_n are unknown weighting coefficients and f_n are basis functions. Substitution of Equation 2.31 into Equation 2.30 yields

$$\sum_{n=1}^{N} a_n L(f_n) \approx g \tag{2.32}$$

where the residual is

$$R = g - \sum_{n=1}^{N} a_n L(f_n) \qquad (2.33)$$

Let us assume that a suitable inner product has been defined for the problem and the boundary conditions are enforced. Equation 2.32 can now take the inner product with a set of weighting functions, or testing functions, w_1, w_2, …, w_m and by requiring the inner product of each testing function with the residual function to be zero this yields (Gibson, 2007)

$$\sum_{n=1}^{N} a_n < w_m , L(f_n) > \; = < w_m , g > \qquad (2.34)$$

and the above Equation 2.34 can now be written in matrix form as:

$$\bar{\bar{Z}} \cdot I = V \qquad (2.35)$$

where $\bar{\bar{Z}} = Z_{mn} = < w_m , L(f_n) >$ and $V = V_m = < w_m , g >$.

Below are some basis functions and testing methods that are commonly used in MoM:

- **Basis functions**
    - Pulse functions
    - Piecewise triangular functions
- **Testing methods**
    - Galerkin’s method

    - Point matching method

2.5 Summary

The existing RT-PACT model and its limitations are discussed in this chapter together with one of the famous numerical solutions, MoM. In Chapter 3, we will introduce the equivalence principle algorithm (EPA) model, an enhanced numerical method based on MoM.

CHAPTER 3

RADIATIVE TRANSFER-EQUIVALENCE PRINCIPLE ALGORITHM (RT-EPA) MODEL

3.1 Equivalence Principle Algorithm

Although MoM numerical technique was famous for its accuracy in solving electromagnetic problems, solving electromagnetic problems directly with MoM will yields high computational cost for memory and time. Due to the limitation of computer memory, MoM was normally restricted to small-scale problems. In this chapter, a new numerical method is introduced which can improve the dense matrix conditioning and enhance the speed of computation where MoM has difficulty to solve.

Equivalence principle algorithm (EPA) is a numerical integral solution method that was developed based on the Huygens's principle, and it states that the tangential components of the fields on a closed surface can be used to evaluate the fields outside or inside the surface (Chenga Lu and Chew, 1995; Li and Chew, 2007). According to Huygens's principle, all points on a wave-front itself can serve as new point sources for the new wavelets and the new wave-front is surface tangential to all secondary wavelets as shown in Figure 3.1.

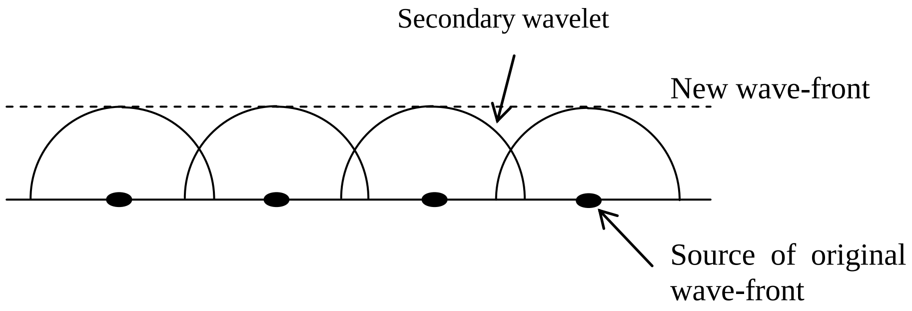

Figure 3.1 Huygens's principle about wave theory.

One of the attractive things about EPA is that it can realize domain decomposition method (DDM) concept to be applied to the integral form of equation. Before that, DDM has been popular with some of the differential form of equation methods like FDM (Lu and Shen, 1997) and FEM (Liu and Jin, 2004) but not with the integral form of equation. The following section will discuss how DDM is applied to the integral form of equation based on equivalence principle.

3.2 Domain Decomposition Method

Domain decomposition method (DDM) provides an attractive solution when dealing with large-scale and complex problems. With DDM, we can decompose a large problem into smaller individual domains and then solve the individual domains independently. With this, DDM allows parallelization in computation, reuse of solution and also improves the matrix conditioning (Li and Chew, 2007). Following is an example of how DDM is applied to decompose a whole big problem into several subproblems based on equivalence principle.

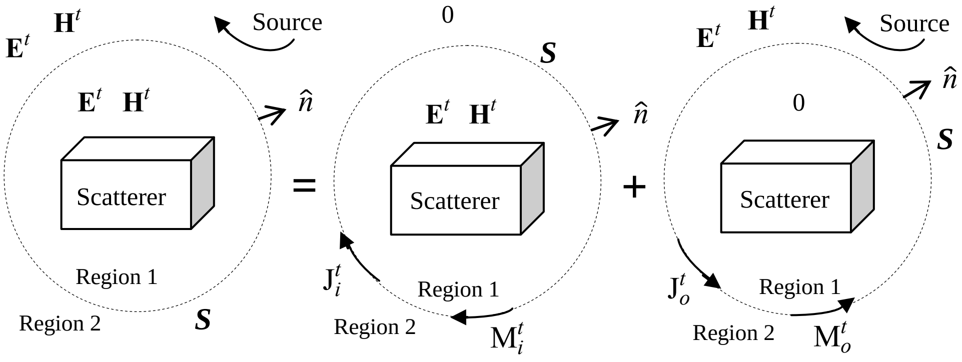

(a) (b) (c)

Figure 3.2 A whole big problem is decomposed into several subproblems using DDM based on equivalence principle.

In Figure 3.2, on the left-hand side, (a) represents the whole big problem and it can be decomposed into two independent subproblems (b) and (c) by using equivalence currents on the equivalence surface *S* of these subdomains (Li and Chew, 2007). Let us consider an incidence wave impinging on a scatterer as shown in Figure 3.2 (a). We then divide the space surrounding the scatterer into two separate regions with a closed equivalence surface *S* with surface normal $\hat{n}$ pointing outward. Inside the *S* is region 1 and outside the *S* is region 2. E^t, H^t are the total electric and magnetic fields defined as $\mathrm{E}^t = \mathrm{E}^i + \mathrm{E}^s$ and $\mathrm{H}^t = \mathrm{H}^i + \mathrm{H}^s$ where the superscripts *i* and *s* denote the incidence and scattered fields.

The method is to decompose the above original problem shown in Figure 3.2 (a) to the two subproblems in Figure 3.2 (b) and Figure 3.2 (c). For Figure 3.2 (b), we need to have the equivalent currents J_i^t, M_i^t on *S* which can generate the incidence fields E^t, H^t inside *S* and zero field outside *S*. Figure below shows how the equivalent currents J_i^t, M_i^t on *S* is generated by having two different equivalent currents operating in opposite direction which are J^i, M^i and J^s, M^s. By adding these two J^i, M^i and J^s, M^s together then we can have the desired equivalent currents J_i^t, M_i^t on *S*.

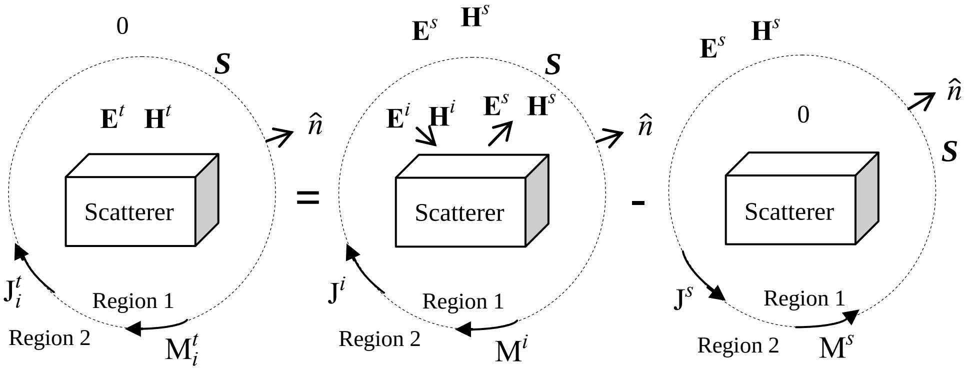

(a) (b) (c)

Figure 3.3 Generate equivalent currents J_i^t , M_i^t on *S* by subtracting an equivalent currents J^i, M^i with another equivalent currents J^s, M^s.

J^i, M^i are equivalent currents on *S* which will generate incidence fields E^i, H^i and scattered fields E^s, H^s inside the *S* and only generate E^s, H^s outside *S* as shown in Figure 3.3 (b). While J^s, M^s are other equivalent currents on *S* that operate in reverse direction to J^i, M^i which will only generate E^s, H^s outside *S* and zero field inside *S* as shown in Figure 3.3 (c). We can now add both the J^i,

M^i and J^s, M^s and finally bring us the J^t_i, M^t_i on S which will only generate E^t, H^t inside S and zero field outside S as shown in Figure 3.3 (a).

After the desired J^t_i, M^t_i is obtained, we can now have another equivalent currents J^t_o, M^t_o which operate against the direction of J^t_i, M^t_i with the original source on. With this, J^t_o, M^t_o will then generate E^t, H^t outside S and zero field inside S as shown in Figure 3.2 (c). If we add the two J^t_i, M^t_i and J^t_o, M^t_o together then we can have the original problem back as shown in Figure 3.2 (a).

By utilizing the DDM scheme, the formulation of EPA can break into three steps via equivalence principle operators and this is discussed in the following section.

3.3 Equivalence Principle Operators

There are three steps involved in equivalence principle operators that need to be performed before scattered field related to the scattered current on an equivalence surface is computed. The first step is called inside-out propagation which describes the process where the original source is replaced by equivalence source that generates the same incidence field inside an equivalent surface but zero field outside. The second step is called solving for the current on the scatterer. At this step, the induced current on the scatterer is computed using MoM. Once the induced current on the scatterer is solved, then the third step is to compute scattered current on the equivalence surface that generate desired scattered field outside but zero field inside.

3.4 EPA Formulation

EPA earned its name as it is based on equivalence principle or also known as Huygens's principle (Chenga Lu and Chew, 1995). The three steps involved in equivalence principle operators discussed at previous section can be written in mathematical form and is discussed in this section. A general form to relate the electric and magnetic currents on an equivalent surface to fields is written as:

$$J = \hat{n} \times H \tag{3.1}$$

$$M = - \hat{n} \times E \tag{3.2}$$

To find the fields outside or inside of a closed surface *S*, we can relate the fields to the tangential components of the fields on an equivalent surface according to equivalence principle and the electric field is written as (Li and Chew, 2007):

$$E(r) = \nabla\times \oint_S dS' g(r-r')\hat{n}(r')\times E_s(r')$$

$$- \frac{1}{i\omega\epsilon} \nabla\times \nabla\times \oint_S dS' g(r-r')\hat{n}(r')\times H_s(r')$$

$$= \nabla\times \oint_S dS' g(r-r')M_s(r') - \frac{1}{i\omega\epsilon} \nabla\times \nabla\times \oint_S dS' g(r-r')J_s(r')$$

$$= K_{EM}^{S}(r,r')M_s(r') + L_{EJ}^{S}(r,r')J_s(r') \tag{3.3}$$

and using duality the magnetic field can be written as (Li and Chew, 2007):

$$H(r) = - K_{HJ}^{S}(r,r')J_s(r') - L_{HM}^{S}(r,r')M_s(r') \tag{3.4}$$

where *K* and *L* are surface operators and are written as (Li and Chew, 2007):

$$L = -\frac{1}{i\omega\epsilon} \nabla\times \nabla\times \oint_S dS' g(r-r') \tag{3.5}$$

$$K = \nabla\times \oint_S dS' g(r-r') \tag{3.6}$$

where *g(r-r')* is the Green's function in the embedding medium and *ω* is angular frequency. The subscript *EM* denotes the electric field and magnetic current while the subscript *EJ* denotes the electric field and electric current. The subscript *HM* denotes the magnetic field and magnetic current while the subscript *HJ* denotes the magnetic field and electric current.

To find the distributed induced current of the scatterer and replace it with equivalent surface current later, let us assume the scatterer is a PEC object. This is because the equivalent surface current that is going to replace the induced current would generate electric and magnetic fields outside the surface but zero inside. By enforcing the boundary conditions on tangential electric field of the PEC object, we can write the total tangential electric field as follow:

$$\hat{t}\cdot E^{sca} = - \hat{t}\cdot E^{inc} \tag{3.7}$$

$$\hat{t}\cdot L_{EJ}^{S}\cdot \mathrm{J}^{ind} = - \hat{t}\cdot E^{inc} \tag{3.8}$$

where $\hat{t}$ denotes an arbitrary tangential vector of the surface, J^{ind} denotes induced current on the surface of scatterer. This current can be solved approximately using MoM method introduced in Chapter 2, Equation 2.35 and can be written as:

$$\bar{Z}\cdot \mathrm{J}^{ind} = E^{inc} \tag{3.9}$$

Using Equation 3.9, then we are able to find the induced current and the scattered field can be computed from equation below:

$$E^{sca} = L_{EJ}^{S}\cdot \mathrm{J}^{ind} \tag{3.10}$$

The three steps involved in equivalence principle operators can then be written in mathematical form as:

$$\begin{bmatrix} \mathrm{J}_s^{sca} \\ \frac{1}{\eta}\mathrm{M}_s^{sca} \end{bmatrix} = \begin{bmatrix} -\widehat{n}' \times K \\ -\frac{1}{\eta}\widehat{n}' \times L \end{bmatrix} \cdot [\bar{Z}]^{-1} \cdot [-L \quad -\eta K] \cdot \begin{bmatrix} \mathrm{J}_s^{inc} \\ \frac{1}{\eta}\mathrm{M}_s^{sca} \end{bmatrix} \tag{3.11}$$

where the $\left[-L \quad -\eta K\right]$ on the RHS is outside-in operator, $[\bar{Z}]^{-1}$ is current solver operator and $\begin{bmatrix} -\widehat{n}' \times K \\ -\frac{1}{\eta}\widehat{n}' \times L \end{bmatrix}$ is inside-out operator.

3.5 Methodology of Theoretical Model Development

EPA is a numerical model that is able to simulate scattered field from a scatterer based on Huygens's principle. In this section, the EPA model will be integrated into existing RT theoretical model for the proposed new improved RT theoretical model which is named as RT-EPA model. As discussed in Chapter 2, in the existing RT theoretical model, the phase matrix of scatterers is normally computed using analytical solution, such as Mie-scattering formulation for spherical scatterer. The phase matrix of spherical scatterer can now be re-calculated using the EPA model. The required components of Stokes matrix in Equation 2.3 for single scatterer which are VV, VH, HV and HH can be simulated using the EPA model. Once the Stokes matrix is solved, then the phase matrix for a unit volume of scatterers can be determined.

To complete a full simulation until the total backscattering is computed with the new RT-EPA model, computations for surface-volume, direct volume and volume-volume scattering have to be identified first at the existing RT theoretical model and the phase matrix is calculated using the EPA model. The simulated results are used to replace the values previously simulated using Mie-scattering formulation. The overview of the development and design of the RT-EPA model is shown as follows:

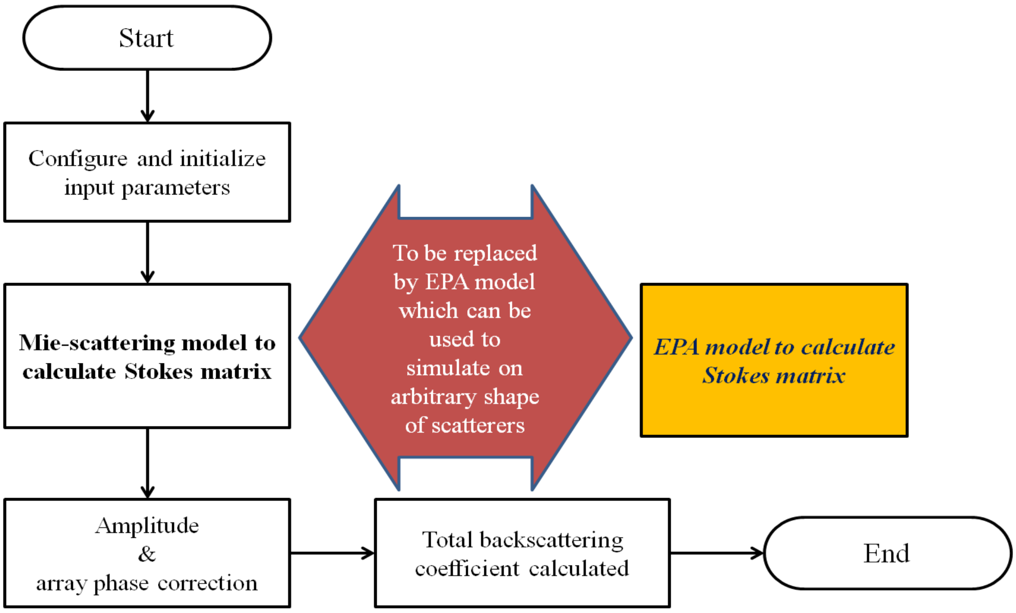

Figure 3.4 Overview of design flow for the proposed RT-EPA theoretical model.

The main modifications involved are in the re-calculation of phase matrix for surface-volume, direct volume and volume-volume scattering shown in Equations 2.25, 2.26, 2.27, 2.28 and 2.29. Re-calculation of volume extinction coefficient in Equation 2.6 together volume scattering coefficient in Equation 2.7 is also needed due to the re-calculation of phase matrix. For the proposed RT-EPA model, the new theoretical model is used to compare with the existing RT theoretical model to determine the accuracy and performance of the numerical method in solving 3D scattering problems for a layer of snow.

Due to several limitations of EPA model like restriction of background permittivity change, absence of magnetic near-field calculation, and longer computational time compared to RHESA model (in Chapter 6), the development of RT-EPA model is focused on spherical scatterers for a layer of snow. For arbitrary shape of scatterers is further discussed at Chapter 5 with the RT-RHESA model.

3.5.1 Phase Matrix for Volume Scattering Coefficient and Volume Extinction Coefficient in the RT-EPA Model

Traditionally, analytical solution with Mie-scattering formulation is used for the phase matrix for a single scatterer in existing RT theoretical model. For this study, the scattered field from a single scatterer in RT-EPA model is now computed using the numerical solution with formulation explained in Section 3.4.

All the required parameters like local incidence angles, scattered angles, frequency, permittivity of the scatterer, radius size of the scatterer and polarizations have to be configured in order to do simulation with the EPA model.

Before the EPA model is used to simulate the scattered field of a single scatterer, there are some steps that have to be performed. The first step is to create the model of spherical scatterer using 3D modeling software like ANSYS. Figure 3.5 shows the 3D model of a spherical scatterer.

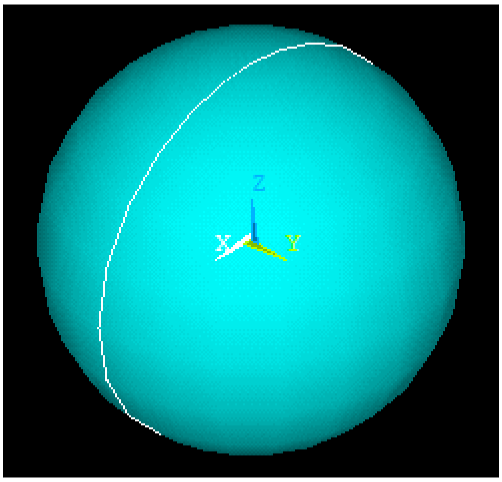

Figure 3.5 A 3D spherical scatterer model created using ANSYS.

Once the spherical scatterer model is created, then it has to be meshed using triangular patches (RWG) defined by the basis function named after Rao-Wilton-Glisson (Rao et al., 1982) and the RWG is used to discretize the surface integral equation if it is a PEC object or if it is a dielectric object, tetrahedral patches (SWG) are used which is defined by the basis function named after Shaubert-Wilton-Glisson (Schaubert et al., 1984) and is used to discretize the volume integral equation if it is a dielectric object.

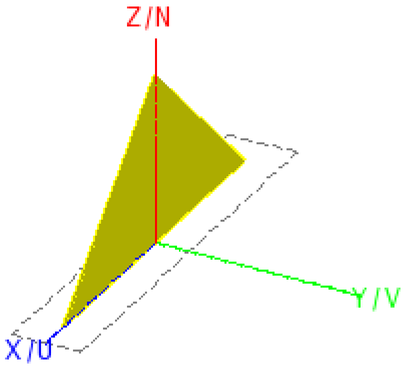

Figure 3.6 Example of a triangular (RWG) that is used to do surface meshing.

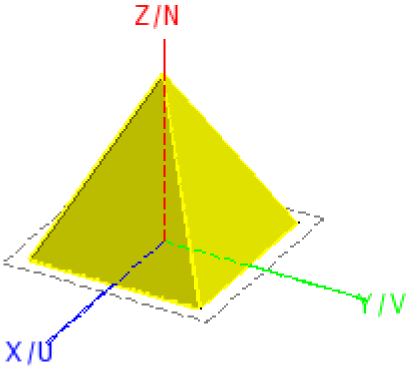

Figure 3.7 Example of a tetrahedral (SWG) that is used to do volume meshing.

Figure 3.6 and Figure 3.7 show the example of triangular (RWG) and tetrahedral (SWG) patches that are used to mesh a spherical scatterer.

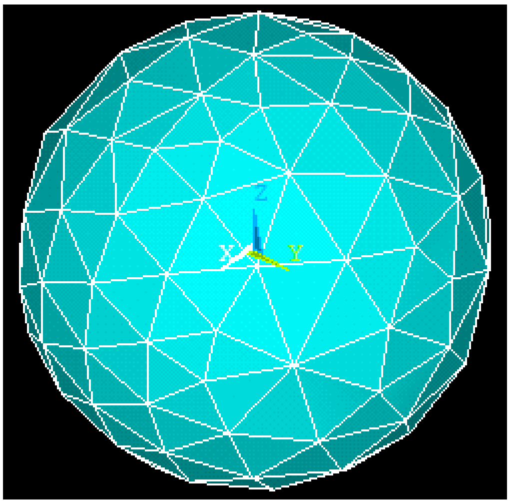

Figure 3.8 Example of a sphere meshed using RWG or SWG.

Figure 3.8 shows a sphere scatterer that is meshed by either using RWG or SWG. Once the scatterer is meshed, then the 3D scatterer model has to be read in by the EPA model before the simulation starts. To start simulation using the EPA model, we have to configure with the parameter values in frequency, permittivity of the scatterer, incidence angles, scattered angles and polarizations. After this, we can now run the simulations for the surface-volume scattering, direct volume scattering, volume-volume scattering, volume extinction coefficient and volume scattering coefficient.

3.5.1.1 Volume Scattering Coefficient and Volume Extinction Coefficient

In this section, we show how the volume scattering coefficient is computed and then used to compute the volume extinction coefficient. Figure 3.9 shows how the simulation is modeled.

The simulated scattered angles for scattered field were sampled using Gaussian quadrature (Kovvali, 2011). The samples of integration points were either 32 points or 64 points for θ and Φ angles, depending on the accuracy needed. The incidence angle can be V or H polarized wave. Once all the scattered field are computed then we can get the volume scattering coefficient using Equation 2.7 by multiplying the results with number of density n_o per unit volume. Using Equation 2.6 and Equation 2.8, substitute the computed volume scattering coefficient then we can get the volume extinction coefficient.

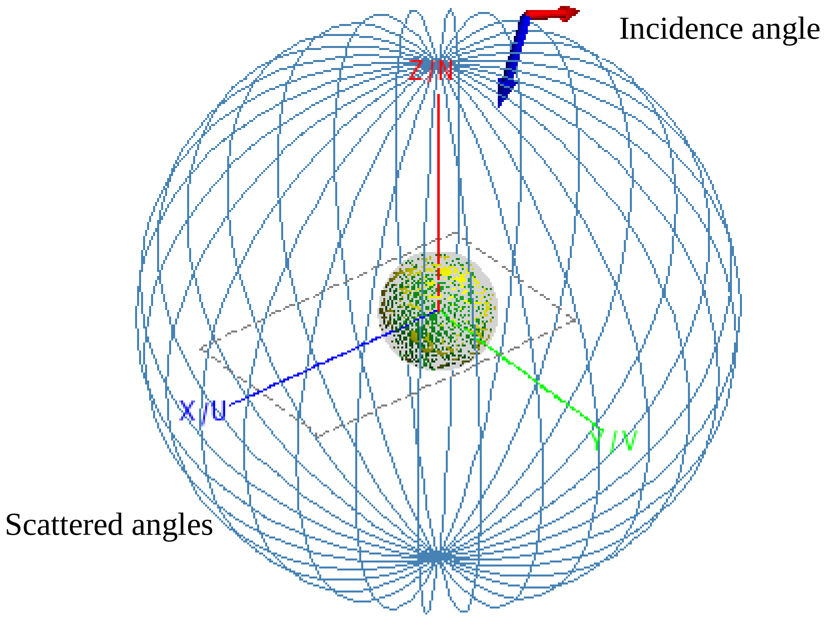

Figure 3.9 Example of simulation configuration of scattering from a sphere.

3.6 Summary

The design and development of the RT-EPA model was discussed in this chapter. In Chapter 4, the RT-EPA model will be used to perform some theoretical analysis and the results are compared with the RT-PACT model.

CHAPTER 4

THEORETICAL ANALYSIS OF RT-EPA MODEL

In this chapter, the developed RT-EPA model discussed in Chapter 3 is used to perform some theoretical analysis to validate further the performance and accuracy of the RT-EPA model within certain parameter range that will be used in the later chapter for ground truth measurement data of the satellite like RADARSAT-1. The RADARSAT-1 satellite microwave SAR operates at 5.30GHz and has been used to collect HH data near Scott Base, Ross Island in Antarctica from 2002 to 2004. The incidence angle of the satellite falls between 24° to 31°.

The EPA model has some of its limitations when simulating different size of scatterer at different frequency especially when the frequency is low and the volume of the scatterer is small which can result in the low-frequency breakdown of EPA (Ma et al., 2011) due to the size of the scatterer is small compared to the wavelength. Besides that, the size of the tetrahedral element (SWG) that is used to mesh the volume of the scatterer has to be reduced when high frequency is used in order to keep the size of the element comparable to the wavelength. The reason for this is it can increase the accuracy with finer mesh. There is a rule of thumb that recommends the average size of the element should be kept at about 1/10 of the wavelength (Tiryaki, 2010).

Following this rule, the total of unknowns can be reduced and this allows faster computational time and speed with better accuracy.

To analyze the accuracy and performance of the EPA model, we adjusted the edge length of the element to find out the possible smallest size allowed by the 3D modeling software while allowing more unknowns (higher total of elements meshed) to increase the accuracy. When there are more unknowns, the computation time will increases. We then tested the edge length with several sizes of scatterers which are 0.5mm, 0.8mm, 1.1mm and 1.5mm and also with several different frequencies which are 1.25GHz, 5.30GHz, 15.50GHz and 35.00GHz.

Adjusting the frequency from lower to higher can change the wavelength of the incidence wave as lower frequency will have a longer wavelength and high frequency will have a shorter wavelength. This can allow us to examine the EPA model whether the low-frequency breakdown could happen with the selected element edge length size that is selected or at what frequency the element edge length size selected can provide better accuracy.

The parameters used for the theoretical analysis are stated below:

Table 4.1 Parameters used in theoretical analysis of a layer of spherical scatterers using the RT-PACT and RT-EPA models.

Parameters	Values Used in Model
Layer Thickness (m)	0.5
Volume Fraction of Scatterer (%)	30
Scatterer Radius (mm)	0.5, 0.8, 1.1, 1.5
Relative Permittivity of Scatterer	(6.9, 0.12)
Background Relative Permittivity	(1.0, 0.0)

.

4.1 Effect of Frequency on Backscattering

Figure 4.1 shows the total backscattering comparison between the RT-PACT and RT-EPA models using configurations stated in Table 4.1. 4 different sizes of spherical scatterer with radius 0.5mm, 0.8mm, 1.1mm and 1.5mm were simulated against 4 different incidence angles for VV polarization for 4 different frequencies which are 1.25GHz, 5.30GHz, 15.50GHz and 35.00GHz.

From Figure 4.1, the results show that all 4 different sizes of scatterers matched well with the RT-PACT. For frequency 35.00GHz, the results for scatterer with radius 1.1mm and 1.5mm have some difference between the two models. This could be because the element edge length size selected is larger compared to the wavelength of incidence wave.

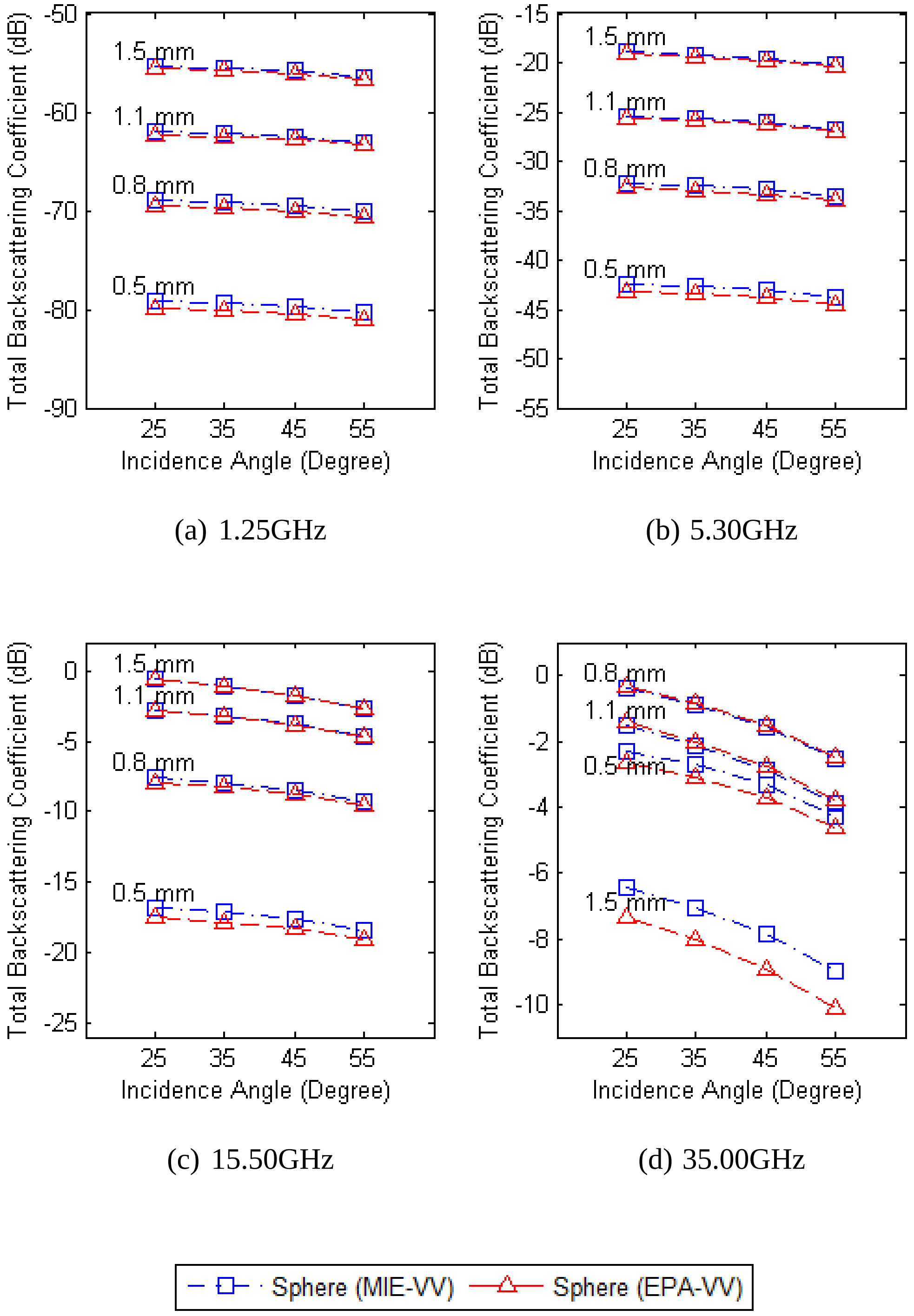

(a) 1.25GHz (b) 5.30GHz

(c) 15.50GHz (d) 35.00GHz

Figure 4.1 Comparison of total backscattering coefficient between the RT-PACT and RT-EPA models against 4 different incidence angles using 4 different sizes of spherical scatterer with radius 0.5mm, 0.8mm, 1.1mm and 1.5mm for VV polarization using 4 different frequencies.

4.2 Effect of Radius of Scatterer on Backscattering

Figure 4.2 shows the comparison of total backscattering coefficient between the RT-PACT and RT-EPA models using configurations stated in Table 4.1. 4 different frequencies which are 1.25GHz, 5.30GHz, 15.50GHz and 35.00GHz are simulated against 4 different incidence angles for VV polarization using 4 different sizes of scatterer with radius 0.5mm, 0.8mm, 1.1mm and 1.5mm. In general, the results from both the models are the same.

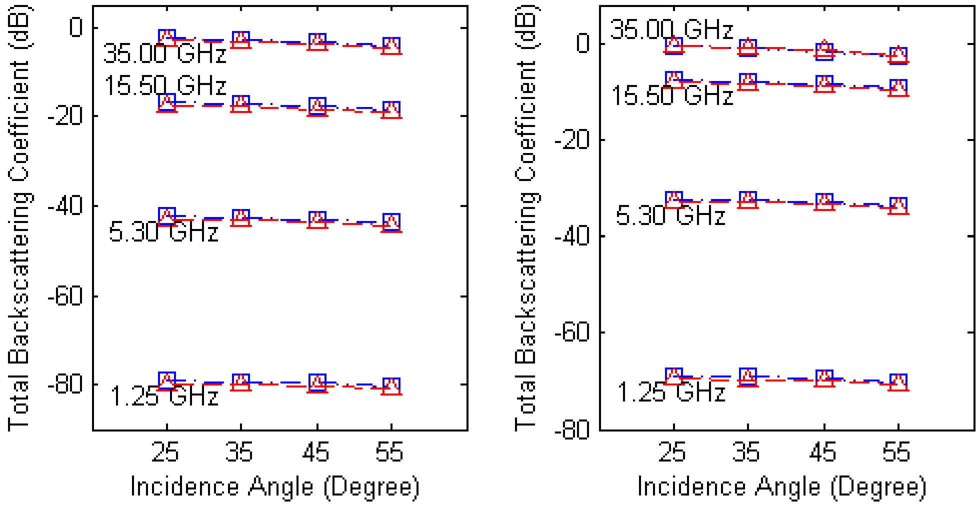

(a) 0.5mm (b) 0.8mm

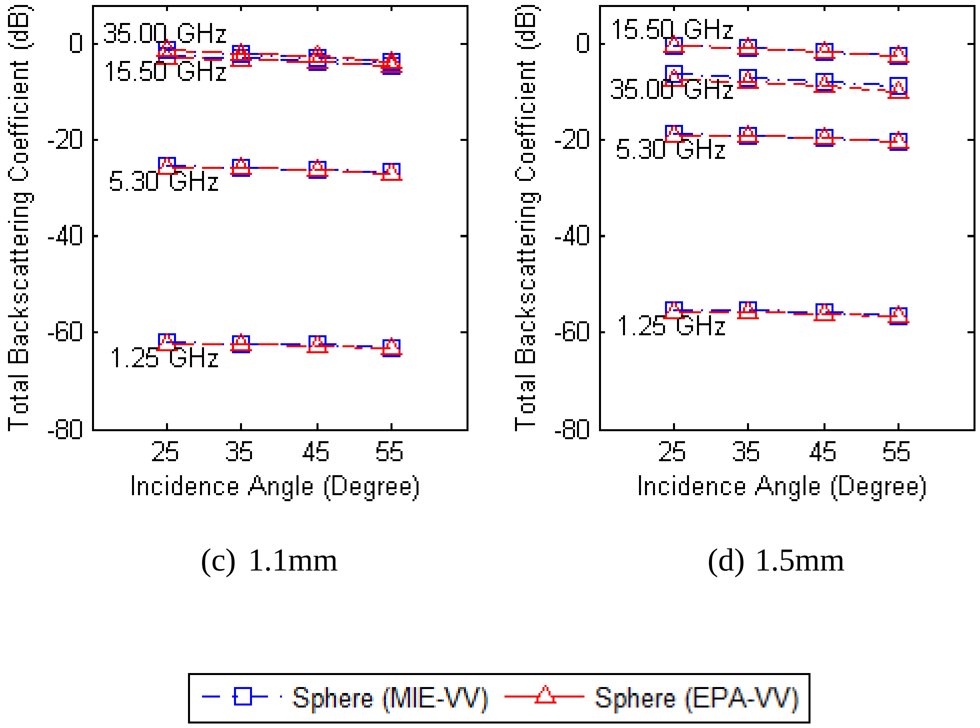

(c) 1.1mm

(d) 1.5mm

Figure 4.2 Comparison of total backscattering coefficient between the RT-PACT and RT-EPA models against 4 different incidence angles using 4 different frequencies which are 1.25GHz, 5.30GHz, 15.50GHz and 35.00GHz for VV polarization using 4 different sizes of spherical scatterer.

4.3 Effect of Incidence Angle on Backscattering

Figure 4.3 shows the comparison of total backscattering coefficient between the RT-PACT and RT-EPA models using configurations stated in Table 4.1. 4 different incidence angles which are 25°, 35°, 45° and 55° are simulated against 4 different frequencies for VV polarization using 4 different sizes of scatterer with radius 0.5mm, 0.8mm, 1.1mm and 1.5mm. In general, the results from both the models are the same.

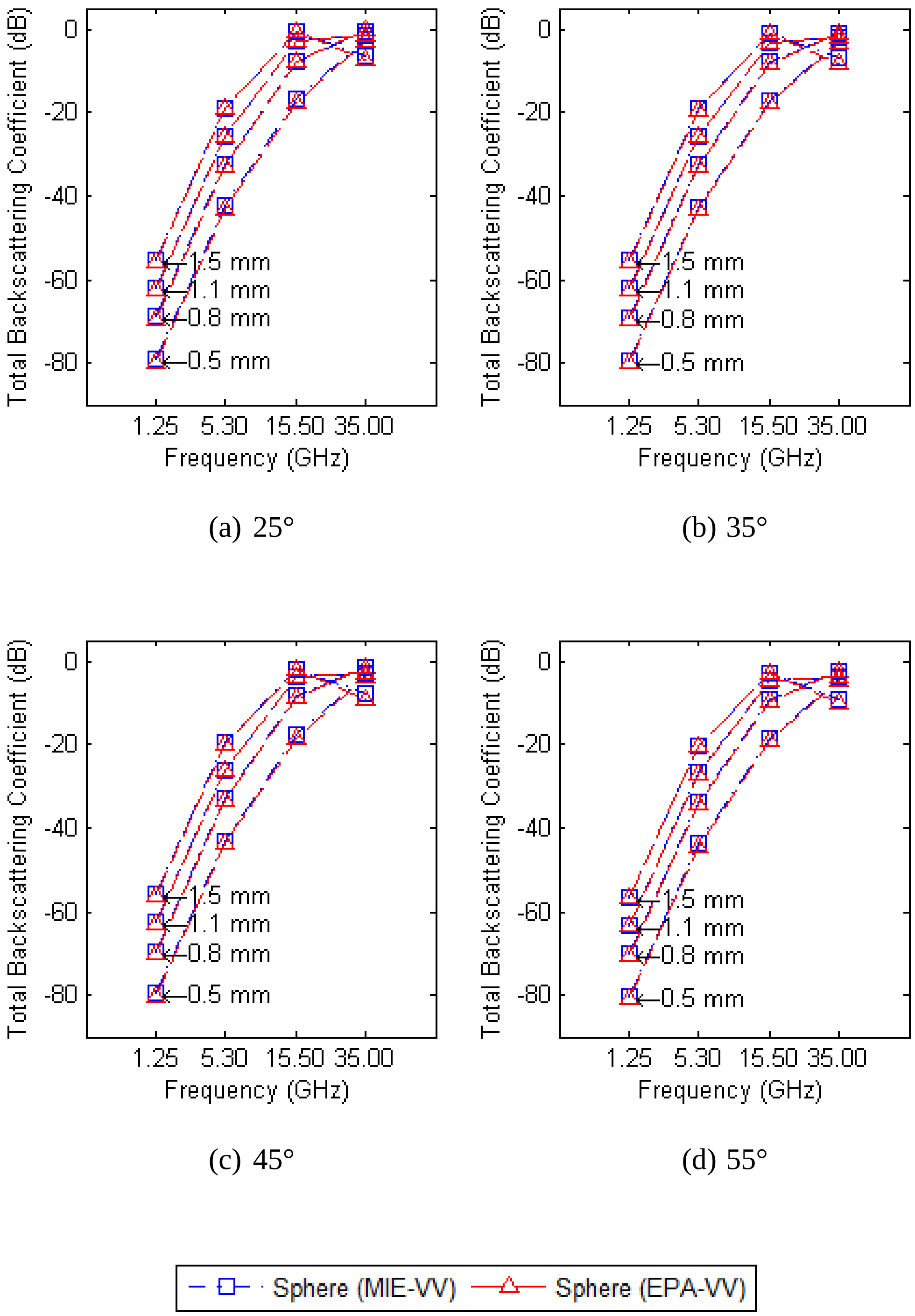

(a) 25°

(b) 35°

(c) 45°

(d) 55°

Figure 4.3 Comparison of total backscattering coefficient between the RT-PACT and RT-EPA models against 4 different frequencies using 4 different incidence angles which are 25°, 35°, 45° and 55° for VV polarization using 4 different sizes of spherical scatterer.

4.4 Summary

The results show that the RT-EPA model matched well with the RT-PACT model. We will continue to discuss the development and simulation of non-spherical shapes of scatterers using the numerical RHESA model in next chapter.

CHAPTER 5

RADIATIVE TRANSFER-RELAXED HIERARCHICAL EQUIVALENT SOURCE ALGORITHM (RT-RHESA) MODEL

5.1 Relaxed Hierarchical Equivalent Source Algorithm (RHESA)

In this chapter, we will introduce a new numerical solution which can provides better accuracy and, faster computational speed. As explained in Chapter 3, the EPA model uses cubical form of equivalence surface to enclose the scatterer. This non-smooth surface with edges and corners could lead to current discontinuity and could induce singular equivalent current on the equivalence surface. Charge singularity could also happen when the equivalence surface intercepts with a scatterer. The discontinuous current between the two pieces of scatterers results in singular charges on the pieces and it is hard to evaluate numerically (Fu et al., 2015). When there are singular fields happen, it can make the simulation result become less accurate. Besides this, the previous implementation of the EPA model does not allow the change of background permittivity of a medium. Thus this has limited the RT-EPA model to be used for other medium like sea ice where brine inclusions can be embedded in the background ice medium.

Relaxed hierarchical equivalent source algorithm (RHESA) is a new implemented numerical approach which is introduced to eliminate the singularities happened in the EPA model and to increase the performance of the EPA (Fu et al., 2016b). The implementation of the RHESA model is based on the EPA foundation. With the new RHESA model, it can provide better accuracy and enhance the computational speed. The RHESA model also allows the change of background permittivity of a medium. Besides this, with the RT-RHESA model, it can be applied to more different kinds of media and save more computational times and resources.

5.1.1 Spherical Equivalence Surface

As the name implies, the word “Relaxed” of RHESA is referred to the relaxed hierarchical arrangement of spherical equivalence surfaces to avoid interception with internal primary sources (Fu et al., 2016a). Using spherical equivalence surface can eliminate the discontinuous current that could happen when a cubical equivalence surface is used. This is because the spherical equivalence surface provides perfect smoothness surface compared to cubical equivalence surface.

Figure 5.1 shows a meshed cubical surface where, the edges and corners of the cubical surface have strong discontinuities (Fu et al., 2015, 2016b). These discontinuities at edges and corners are one of the causes of the singular equivalent current in the EPA model.

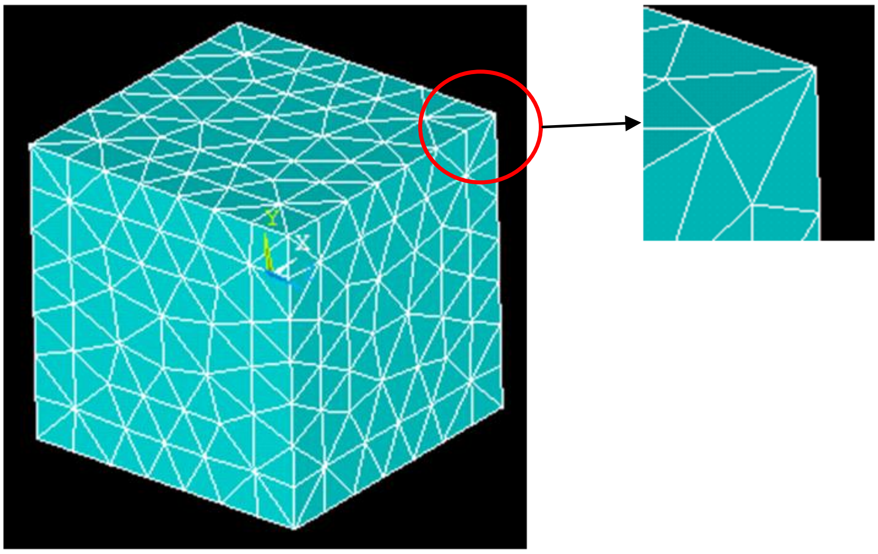

Figure 5.1 Discontinuities at edges and corners of a meshed cubical equivalence surface.

Spherical surface can provide perfect smoothness as there are no edges and corners compared to cubical surface. With no discontinuous current at edges and corners of equivalence surface, it can increase the accuracy compared to cubical surface. The study of comparing the benefit of spherical surface compared to cubical surface (Fu et al., 2016b) has shown that the spherical surface can increase the accuracy and avoid singularities caused by non-smoothness surface.

5.2 RHESA Formulation

In this section, we will discuss about the formulation of the RHESA model. For dielectric scatterer, applying volume integral equation (VIE) can produce a lot of unknowns when discretizing the scatterer. The RHESA can reduce the total number of unknowns to be solved by using hierarchical form of equivalent source algorithm (ESA) (Li et al., 2017).

Although MoM has been famous in solving 3D field scattering problems numerically but some of its limitations such as the implementation complexity and the difficulty in solving dense matrix equation has made it less popular in solving volume integral equation. Thus, a new way of implementing the MoM formulation for VIE has been introduced in this RHESA model. The original MoM volume integral equation that relates the unknown coefficients of current to the excitation vector is written as follows (Fu et al., 2016a):

$$\bar{\bar{Z}} \cdot I = V \tag{5.1}$$

where $\bar{\bar{Z}}$ is the impedance matrix, I is the unknown coefficients vector and V is the excitation vector.

For dielectric scatterer, applying the above volume integral equation directly can yield a lot of unknowns when discretizing a scatterer. The RHESA can reduce the total of unknowns to be solved by using hierarchical form of ESA. With the help of hierarchical form of ESA, the above equation can be rewritten as follows (Fu et al., 2016a):

$$\bar{\bar{Z}} \cdot I = \bar{\bar{Z}}_{near} \cdot I + \bar{\bar{Z}}_{far} \cdot I \tag{5.2}$$

The $\bar{Z}$ impedance matrix is distributed into two groups which are near-field ($\bar{Z}_{near}$) group and far-field ($\bar{Z}_{far}$) group interactions. The near-field interactions between groups will be solved directly through MoM while the far-field interactions between groups will be solved and accelerated by using the hierarchical form of ESA before MoM is applied.

Figure 5.2 shows the forming of hierarchical form of ES (equivalence surface) over a strip. The scatterer is first divided into small groups using cubical box to form the lowest level of oct-tree. The benefit of using cubical box at the lowest level of oct-tree is because the scatterer can be divided into smaller groups without any overlapping. Each cube is then enclosed by a spherical equivalence surface (ES) to form the upper level of oct-tree without touching the cube and the internal primary sources. The upper layer of ESs becomes the parent groups (ES^p) of the child groups (ES^c) of ESs that form below it.

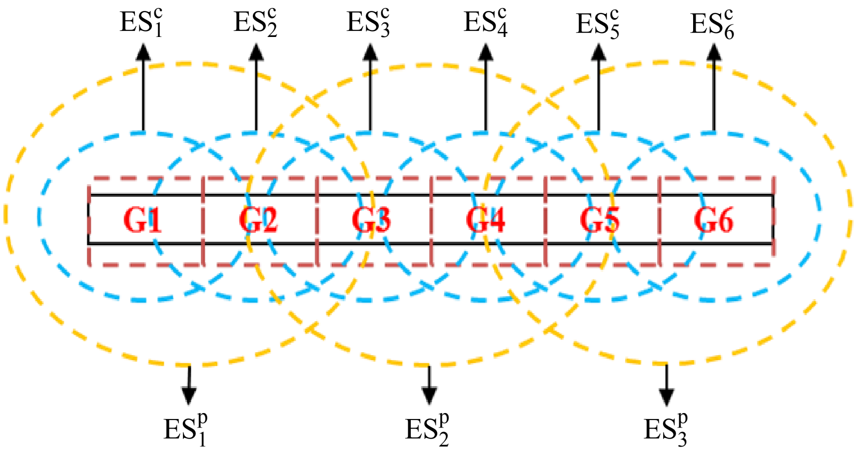

Figure 5.2 Construction of child groups (ES^c) and parent groups (ES^p) of equivalent sources using spherical equivalence surfaces.

For the far-field computation, the RHESA model uses the ESA which involves the following three steps: inside-out radiation, translation and outside-in radiation (Fu et al., 2016a), as shown in Figure 5.3:

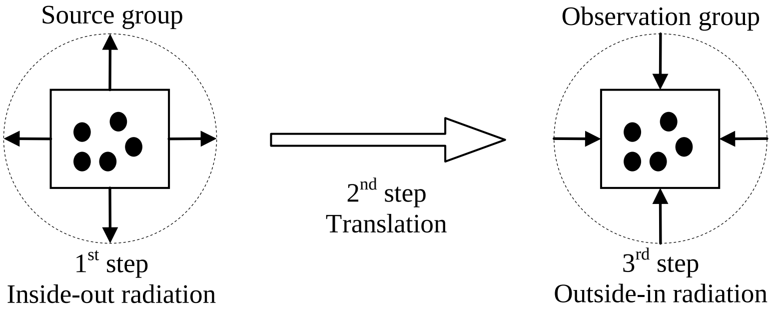

Figure 5.3 Far-field contributions from source group G^s to observation group G^o via ESA: inside-out radiation, translation and outside-in radiation. The spheres inside both groups represent the equivalent sources.

5.2.1 Inside-out Radiation

After breaking the scatterer into smaller groups and establishing the constructs of oct-tree, the RHESA model will first performs the inside-out radiation from lower levels ESs to upper levels ESs at the source group G^s. At this step, the original sources that generate incidence electric and magnetic fields are replaced by the equivalent sources on the ESs of the source group G^s by following the surface equivalence principle. The radiation of field of each level from child group to parent group is conducted using Stratton-Chu integral formulation (Stratton and Chu, 1939; Fu et al., 2016a).

As discussed in Chapter 3, the EPA formulation, the equivalence current on a surface that encloses a scatterer can be related to the primary source inside the surface using two of the field integral operators which are electric field surface operator (L) and magnetic field surface operator (K).

At RHESA, this process could refer to a group of equivalent sources and is enclosed entirely by a virtual ES. The electric and magnetic fields that are generated on this ES can be considered as the contributions from these sources. The electric and magnetic fields on the ES can be written as (Fu et al., 2016a):

$$E = L(J(r')) \tag{5.3}$$

$$H = K(J(r')) \tag{5.4}$$

$$J = \hat{n} \times H, \; p_e = \hat{n} \cdot E \tag{5.5}$$

$$M = -\hat{n} \times E, \; p_m = \hat{n} \cdot H \tag{5.6}$$

where p_e is equivalent electric charge density and p_m is equivalent magnetic charge density.

5.2.2 Translation

When the inside-out radiation of all the equivalent sources inside the source group G^s has been considered and computed, the process then reaches to the top layer of ES that encloses all the equivalent sources inside the source group G^s. The contribution from the source group G^s to the observation group G^o process is called translation. In this step, the field from the source group G^s radiated to the observation group G^o is calculated using the Stratton-Chu integral formulation written as follows (Stratton and Chu, 1939; Fu et al., 2016a):

$$
\begin{aligned}
E(r) &= \int_S \left[ik\eta g(r,r')J_s(r')+M_s(r')\times \nabla g(r,r')-p_e(r')\nabla g(r,r')\right]dr' \\
&= C_E(J_s,M_s,p_e) \qquad (5.7)
\end{aligned}
$$

$$
\begin{aligned}
H(r) &= \int_S \left[-\frac{ik}{\eta} g(r,r')M_s(r')+J_s(r')\times \nabla g(r,r')-p_m(r')\nabla g(r,r')\right]dr' \\
&= C_H(J_s,M_s,p_m) \qquad (5.8)
\end{aligned}
$$

where C_E and C_H represent the integral operators for electric and magnetic fields in terms of currents and charges, respectively.

Once the field radiation from the source group G^s to the observation group G^o is completed, it then moves to the last step called the outside-in radiation.

5.2.3 Outside-in Radiation

The third step, the outside-in radiation, is the last step of computing the far-field interactions. This process is similar to the inside-out radiation but operate in opposite direction where the field radiation is from upper levels ESs to lower levels ESs in the observation group G^o. At this stage, the equivalent sources on the ES of the observation group G^o are updated with the radiated field from the source group G^s after the translation process discussed in the previous section using the Stratton-Chu integral formulation which then generate the electric and magnetic fields inside the ES. When it reaches the lowest level of child group, the calculation of far-field contributions from group G^s to group G^o is completed (Fu et al., 2016a).

The RHESA model uses spherical surface with perfect smoothness to avoid the singularities that happen in the EPA model and uses the hierarchical form of ES to accelerate the far-field computation. This makes it to be a more attractive solution compared to the EPA model. Besides this, using spherical surface also allows the meshless integral scheme, Gauss-Legendre quadrature rule, to be applied. With this new meshless method, it can avoid any element-based mesh and thus can provide an error-free solution to the problems caused by element size irregularities and mesh defect (Fu et al., 2015).

5.3 Methodology of Theoretical Model Development

The overall development of the RT-RHESA theoretical model is shown in Figure 5.4.

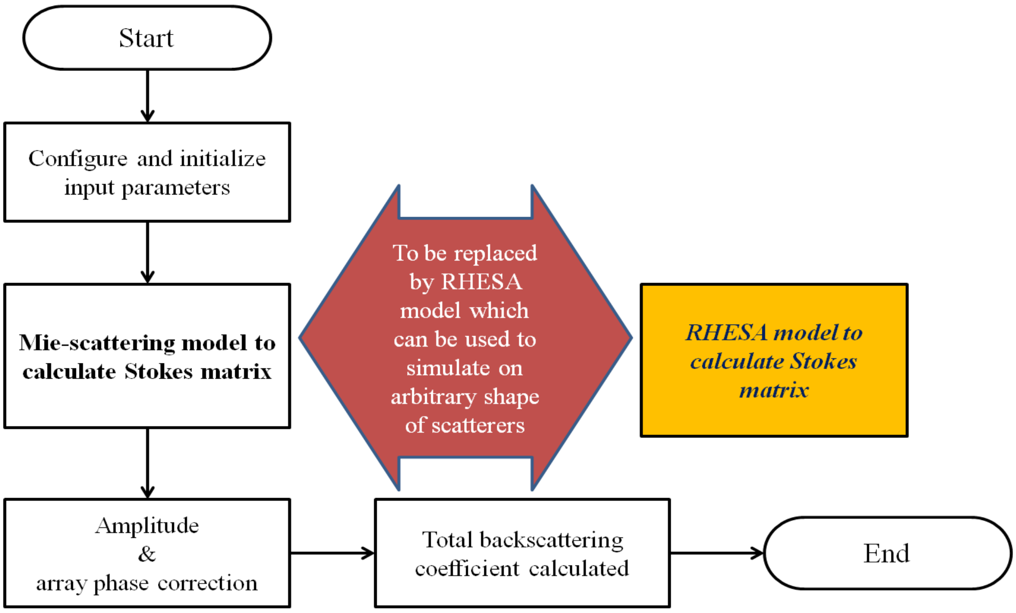

Figure 5.4 Overview of design flow for the proposed RT-RHESA theoretical model.

The new RT-RHESA model continues to go through a series of processes that are already discussed in Chapter 3 for the RT-EPA model. The REHSA model is now used to replace the Mie-scattering of the EPA model to calculate the Stokes matrix. Different kinds of shapes of scatterers like cylinder and peanut shapes are going to be simulated using the RT-RHESA model for a layer of snow. Other shapes of scatterers can be considered and this extends the capability of existing RT-PACT model that uses standard shapes of scatterers.

Generally when simulating a medium that is embedded with non-spherical scatterers with various distributions of orientation angles, all the information about angular scattering by that medium should contain all the 16 elements of its scattering matrix but this is not always the case. A media with rotational symmetry or with higher symmetry can further reduce the number of independent, nonzero elements (Bohren and Huffman, 1983; Mishchenko et al., 2002; Kokhanovsky, 2013). The 16 nonzero elements scattering matrix has a form written as follows (Ulaby et al., 1986; Fung, 1994):

$$\begin{bmatrix} S_{11} & S_{12} & S_{13} & S_{14} \\ S_{21} & S_{22} & S_{23} & S_{24} \\ S_{31} & S_{32} & S_{33} & S_{34} \\ S_{41} & S_{42} & S_{43} & S_{44} \end{bmatrix} \tag{5.9}$$

where S_{ij} (i,j = 1,2,3,4) are the elements of scattering matrix which are derived from the amplitude scattering matrix elements (Ulaby et al., 1986; Fung, 1994) (APPENDIX A). The above scattering matrix can be used to relate the scattered intensity to the incidence intensity via Stokes parameters (Equation 2.2) known as the phase matrix P (Ulaby et al., 1986),

$$\mathrm{I}^s = \frac{1}{4\pi} P\, \mathrm{I}^i \tag{5.10}$$

where superscripts i and s refer to the incidence and scattered intensity.

The phase matrix in Equation 2.3 is used for spherical scatterer and is a simplified matrix with a 2 × 2 dimensions. Due to the spherically symmetric of a scatterers, the 4 × 4 phase matrix for a collection of scatterers can have a form written as follows (Bohren and Huffman, 1983; Mishchenko et al., 2000, 2002; Kokhanovsky, 2004; Liou et al., 2016):

$$\begin{bmatrix} S_{11} & S_{12} & 0 & 0 \\ S_{21} & S_{22} & 0 & 0 \\ 0 & 0 & S_{33} & S_{34} \\ 0 & 0 & S_{43} & S_{44} \end{bmatrix} \tag{5.11}$$

Equation 5.11 is also a well-known block-diagonal structure for an ensemble of scatterers having a plane of symmetry or rotational symmetry. The scattering matrix consists of eight nonzero elements and only six of them are independent. For most of the applications only like and cross polarizations are of interest. Thus, the first four elements of the phase matrix are extracted to define the elements of the 2 × 2 matrix in Equation 2.4 (Jin, 1993; Fung, 1994).

Generally the phase matrix for a collection of non-spherical scatterers should involve all the 16 elements (APPENDIX A). For a medium that has a mixture of scatterers with different shapes and orientations, the phase matrix has to be averaged over orientation angles α and β of the scatterer (Jin, 1993; Fung, 1994). The rotation angles α and β of a scatterer can be found in APPENDIX A.

Due to the complexity of implementing a full 16-elements phase matrix, problems such as the volume of the irregular shape of scatterer is difficult to be calculated and also the computational time for various distribution of orientations angles is very time consuming using the RHESA model, thus, the study of this research has selected the shape of scatterer to have at least a plane of symmetry, identical in size and aligned to Z axis. With this, a medium can now be considered as a macroscopically isotropic and mirror-symmetric (ISM) (Mishchenko et al., 2000, 2002, 2006; Liou et al., 2016) scattering medium and has the well-known block-diagonal structure as written in Equation 5.11.

Besides this, the scattering coefficient $\overline{\overline{K}}_s$ and absorption coefficient $\overline{\overline{K}}_a$ for an ISM medium is independent of incidence direction and can be in scalar form (Ao, 2001) as written in Equation 2.7 and Equation 2.8. This can help to reduce further the computational time needed.

The simulation for a layer of snow using the RT-RHESA model will involve all the scattering mechanisms discussed in Chapter 3. The total number of calculation based on incidence angles and scattered angles needed for each scattering mechanism which involve volume scattering are listed in the table below:

Table 5.1 Total incidence angles and scattered angles have to be simulated by the RT-RHESA model for the listed scattering mechanisms which involve a scatterer.

Contribution Terms	Incidence Angles	Scattered Angles
Volume Extinction	1	2048
Volume-Surface Coherent (m → s)	1	1
Volume-Surface Coherent (s → m)	1	1
Volume-Surface Non-Coherent (m → s)	1	1024
Volume-Surface Non-Coherent (s → m)	1024	1
Volume (up, down)	1	1
Volume (up, up, down)	1025	1025
Volume (up, down, down)	1025	1025
Total	3079	5126

5.4 Summary

The design and development of the RT-RHESA model is discussed in this chapter. In Chapter 6, we will discuss some of the results collected from the theoretical analysis performed using the RT-RHESA model. From the theoretical analysis results, we compared different kinds of shapes of scatterers such as sphere, cylinder and peanut shapes to see the effect of shape on total backscattering for different shapes of scatterers and also study the effect of frequency, layer thickness and volume fraction on these selected shapes.

CHAPTER 6

THEORETICAL ANALYSIS OF RT-RHESA MODEL

In this chapter, the developed RT-RHESA model that was discussed in Chapter 5 is used to perform some theoretical analysis using different kinds of shapes of scatterers such as cylinder and peanut shapes for a layer of snow.

With the new RT-RHESA model, the model can now be applied to different kinds of shapes of scatterers and to study backscattering from a layer of snow with different kinds of shape of scatterers. This could provide clues or better understanding of scattering pattern or scattering behavior of each type of scatterers that can be identified and could be used for future studies of earth terrain like snow or sea ice.

Simulating a layer of snow with different shapes is one of the scopes to be achieved in this study. As mentioned in Chapter 2, particles inside the snow layer could be different from time to time and not always in spherical form. Thus, in the later section, the results of theoretical analysis using 3 different kinds of shapes which are sphere, cylinder and peanut shapes will be discussed.

The parameters used for the theoretical analysis are stated below:

Table 6.1 Parameters used for theoretical analysis in Sections 6.1 and 6.2 for a layer of snow using the RT-PACT and RT-RHESA models.

Parameters	**Values Used in Model**
Relative Permittivity of Scatterer	(3.15, 0.001)
Layer Thickness (m)	0.5
Volume Fraction of Scatterer (%)	20
Scatterer Shape	Sphere, Cylinder, Peanut
Relative Permittivity of Top Layer	(1.0, 0.0)
Background Relative Permittivity	(1.0, 0.0)
Relative Permittivity of Bottom Layer	(6.0, 0.0)
Top Surface RMS Height, Correlation Length	0.12cm, 0.7cm
Bottom Surface RMS Height, Correlation Length	0.06cm, 0.45cm

Table 6.2 Parameters used for theoretical analysis in Sections 6.1 and 6.4 for a layer of snow using the RT-PACT and RT-RHESA models.

Parameters	**Values Used in Model**
Relative Permittivity of Scatterer	(3.15, 0.001)
Layer Thickness (m)	0.1m, 0.5m 5.0m
Volume Fraction of Scatterer (%)	20, 30, 40
Scatterer Shape	Sphere, Cylinder, Peanut
Relative Permittivity of Top Layer	(1.0, 0.0)
Background Relative Permittivity	(1.0, 0.0)
Relative Permittivity of Bottom Layer	(6.0, 0.0)
Top Surface RMS Height, Correlation Length	0.12cm, 0.7cm
Bottom Surface RMS Height, Correlation Length	0.06cm, 0.45cm

Figure 6.1 shows the 3 selected shapes of scatterers used for the theoretical analysis:

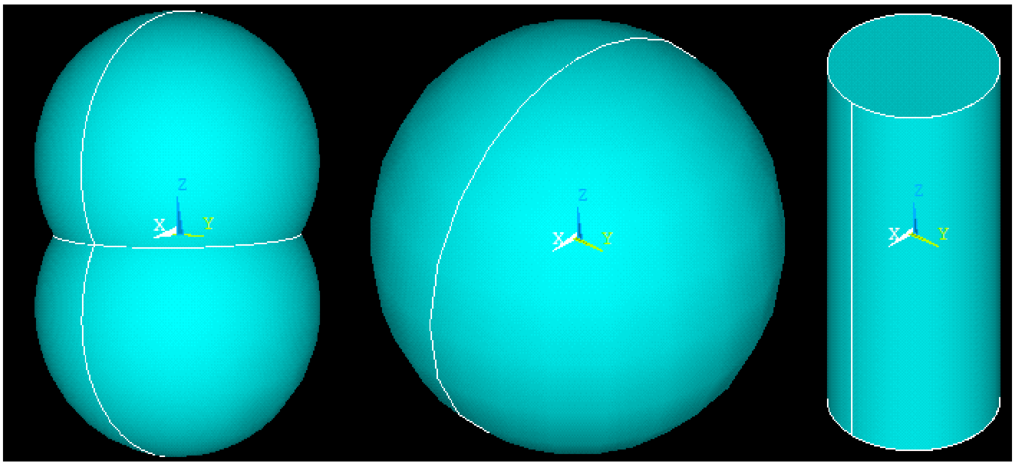

Figure 6.1 Shapes selected for scatterers used in theoretical analysis.

6.1 Effect of Shape of Scatterer on Backscattering

Figure 6.2 shows the comparison of total backscattering between the RT-PACT and RT-RHESA model using 3 different shapes of scatterers which are sphere, cylinder and peanut for VV and HH polarizations. The parameters used for this simulation is stated in Table 6.1. The results for sphere shape are simulated using the RT-PACT model while the results for cylinder and peanut shapes are simulated using the RT-RHESA model. The frequency used is 15.50GHz. There are total 6 incidence angles selected for the simulations. The size of the sphere radius is 0.54mm. The size of the cylinder used in the simulation is 0.35mm radius and 1.7mm length and the peanut shape of scatterers is actually a combination of two spherical scatterers of 0.45 mm radius each with the combined length of 1.36mm.

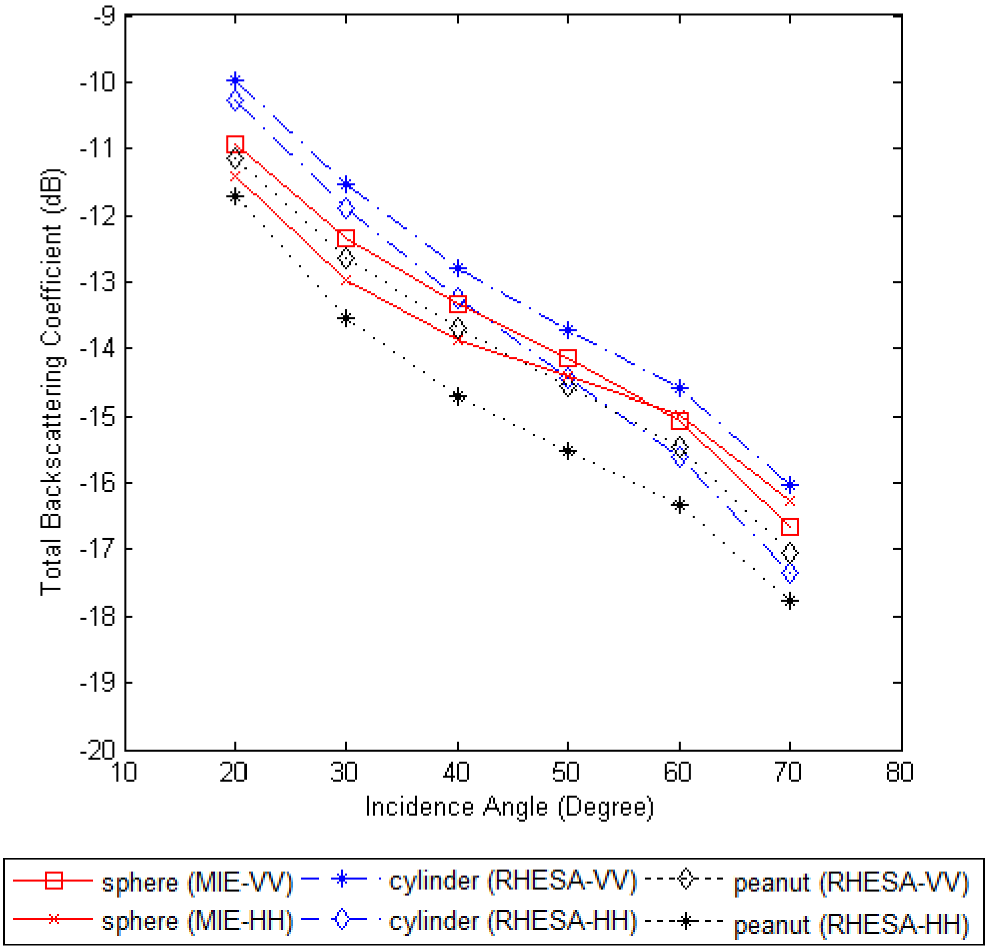

Figure 6.2 Total backscattering comparison between the RT-PACT and RT-RHESA model against 6 different incidence angles with 3 different shapes of scatterers for VV and HH polarizations using frequency 15.50GHz.

The results show that the cylinder shape has a higher total backscattering coefficient compared to others. There are more differences between each shape especially when the incidence angles are between 50° to 70°. The cylinder shape gives bigger separation between VV and HH polarizations when the incidence angles are between 50° to 70°.

Figure 6.3 shows the comparison of total backscattering between the RT-PACT and RT-RHESA model using 3 different shapes of scatterers which are sphere, cylinder and peanut for VH polarization using the same configuration of parameters and same size of scatterers as in previous Figure 6.2. The sphere shape gives a higher total backscattering coefficient compared to others. A higher total backscattering coefficient for VH could mean there are more multiple scattering within the medium.

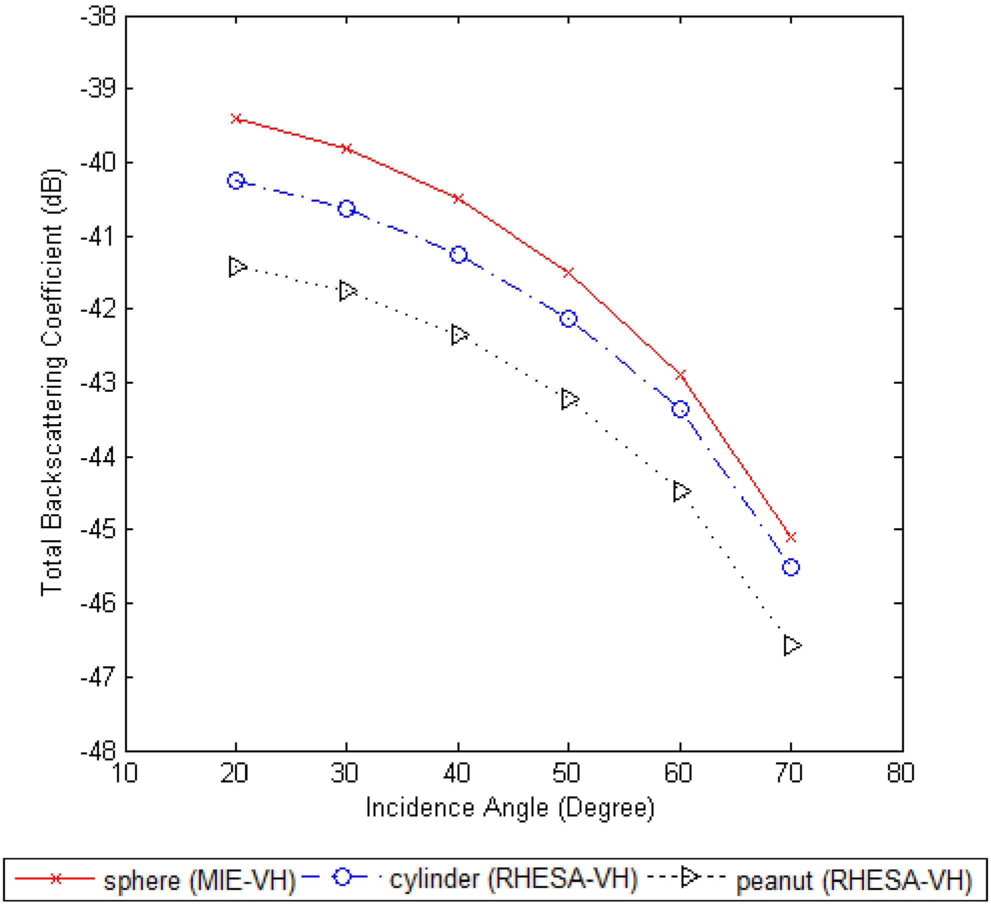

Figure 6.3 Total backscattering comparison between the RT-PACT and RT-RHESA model against 6 different incidence angles with 3 different shapes of scatterers for VH polarization using frequency 15.50GHz.

6.2 Effect of Frequency for Different Shapes of Scatterer on Backscattering

Figure 6.4 shows the comparison of total backscattering between the RT-PACT and RT-RHESA model using 3 different shapes of scatterers which are sphere, cylinder and peanut for VV and HH polarizations. The parameters used for this simulation is stated in Table 6.1. The results are simulated using 3 different frequencies which are 5.30GHz, 15.50GHz and 35.00GHz. The results for sphere shape are simulated using the RT-PACT model while the results for cylinder and peanut shapes are simulated using the RT-RHESA model. There are total 6 incidence angles selected for the simulations. The sizes of the scatterers for the 3 selected shapes are the same as in previous Figure 6.2.

At frequency 5.30GHz, all the 3 different shapes of scatterers show a quite similar scattering pattern. This makes the 3 shapes harder to be differentiated when the frequency is not high as the wavelength is much bigger compared to the size of the scatterer. At frequencies 15.50GHz and 35.00GHz, the differences between cylinder, peanut and sphere shapes scattering patterns are more noticeable. This is because the cylinder and peanut shapes have a smaller radius size and only can be seen by the incidence wave when the wavelength becomes comparable to the size of the scatterer. Besides this, as the incidence angle increases, the volume scattering become dominant for cylinder and peanut shapes compared to sphere as this two shapes give bigger separations between VV and HH polarizations.

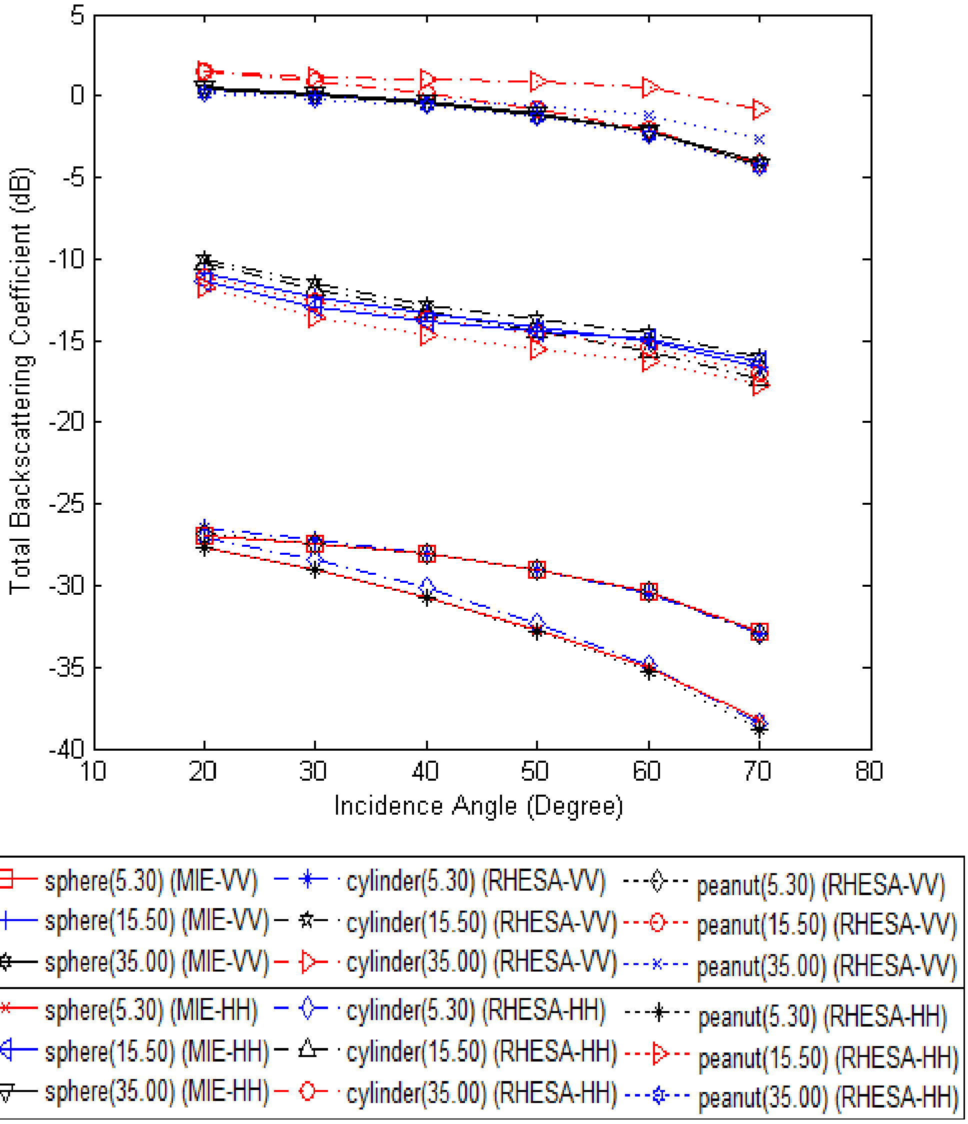

Figure 6.4 Total backscattering comparison between the RT-PACT and RT-RHESA model against 6 different incidence angles with 3 different shapes of scatterers for VV and HH polarizations using 3 different frequencies (5.30GHz, 15.50GHz, 35.00GHz).

Figure 6.5 shows the comparison of total backscattering between the RT-PACT and RT-RHESA model using 3 different shapes of scatterers which are sphere, cylinder and peanut for VH polarization using the same configuration of parameters and same size of scatterers as Figure 6.4. In general, the results from the 3 different shapes of scatterers are the same.

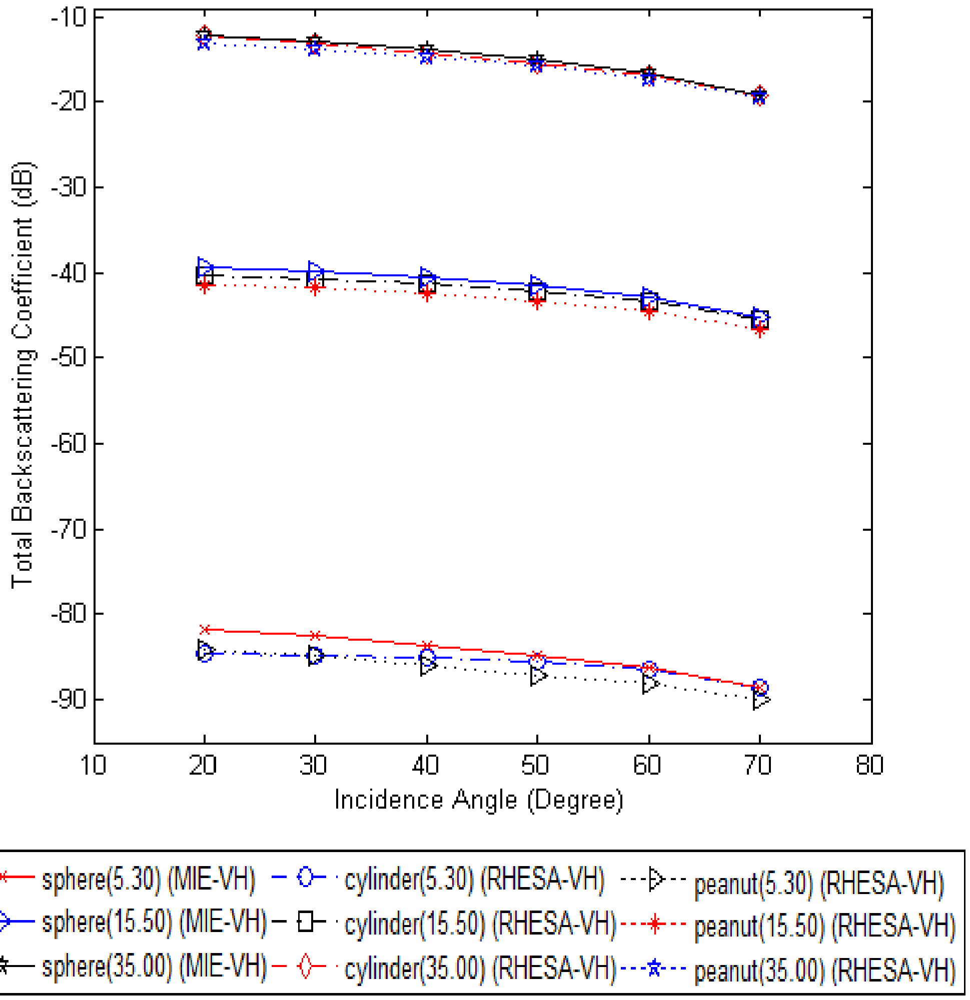

Figure 6.5 Total backscattering comparison between the RT-PACT and RT-RHESA model against 6 different incidence angles with 3 different shapes of scatterers for VH polarization using 3 different frequencies (5.30GHz, 15.50GHz, 35.00GHz).

6.3 Effect of Layer Thickness for Different Shapes of Scatterer on Backscattering

Figure 6.6 shows the comparison of total backscattering between the RT-PACT and RT-RHESA model using 3 different shapes of scatterers which are sphere, cylinder and peanut for VV and HH polarizations. The parameters used for this simulation is stated in Table 6.2. The results are simulated using 3 different layers of thicknesses which are 0.1m, 0.5m and 5.0m. The frequency used is 15.50GHz. The results for sphere shape are simulated using the RT-PACT model while the results for cylinder and peanut shapes are simulated using the RT-RHESA model. There are total 6 incidence angles selected for the simulations. The sizes of the scatterers for the 3 selected shapes are the same as in previous Figure 6.2.

We notice that the cylinder shape gives higher total backscattering coefficient at smaller incidence angles between 20° to 40° for layer thickness at 0.5m and 5.0m. At layer thickness of 0.1m, results show a quite similar scattering pattern among the 3 different shapes as the layer thickness is small and contributions to total backscattering is mainly from surface scattering. When the layer thickness is 5.0m, as the incidence angle increases there are more contributions from the volume scattering by the cylinder and peanut shapes compared to the sphere shape. The sphere shape gives a higher HH than the VV polarization when the incidence angles are large and this means the contributions are dominant by the surface-volume interactions.

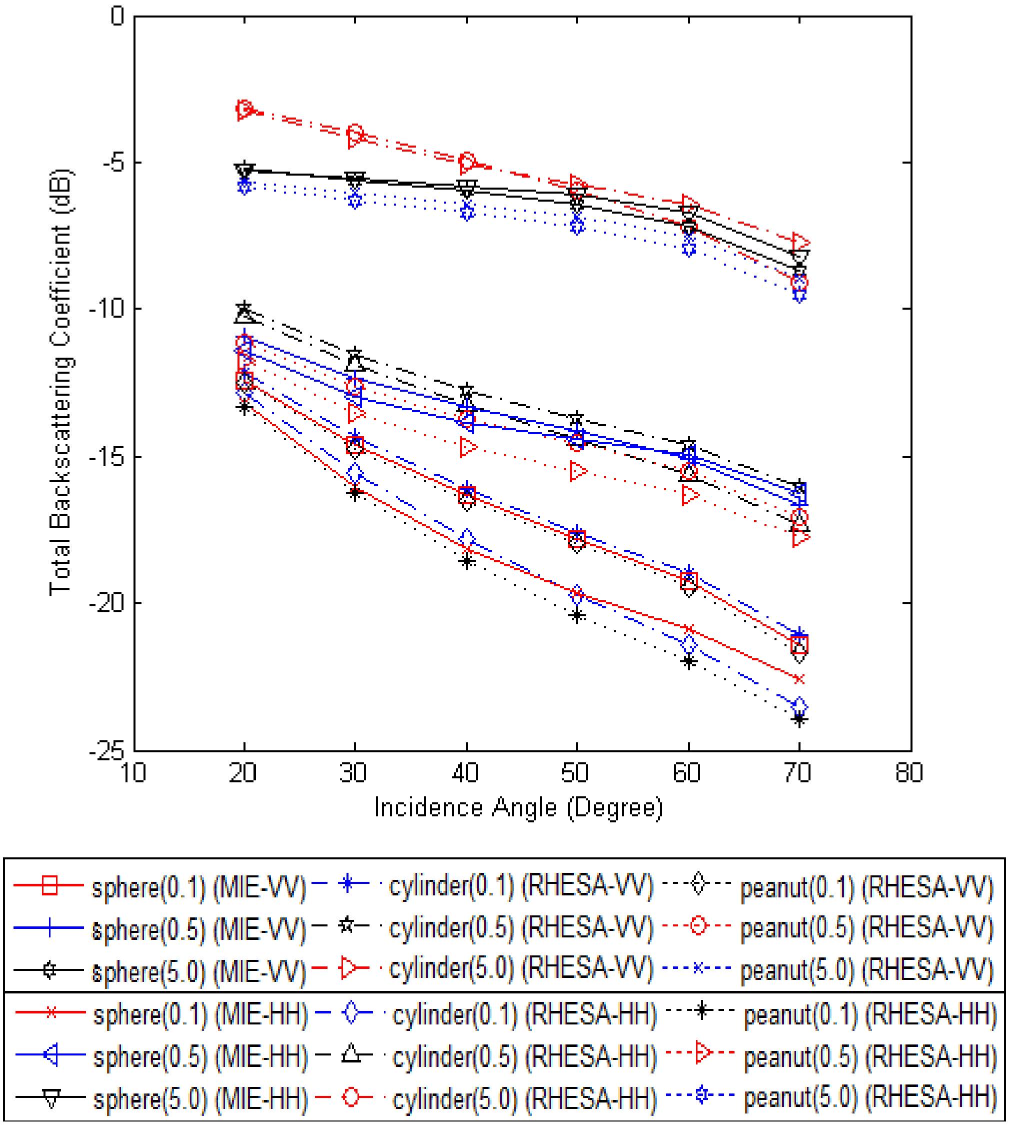

Figure 6.6 Total backscattering comparison between the RT-PACT and RT-RHESA model against 6 different incidence angles with 3 different shapes of scatterers for VV and HH polarizations using frequency 15.50GHz and 3 different layer thicknesses (0.1m, 0.5m, 5.0m).

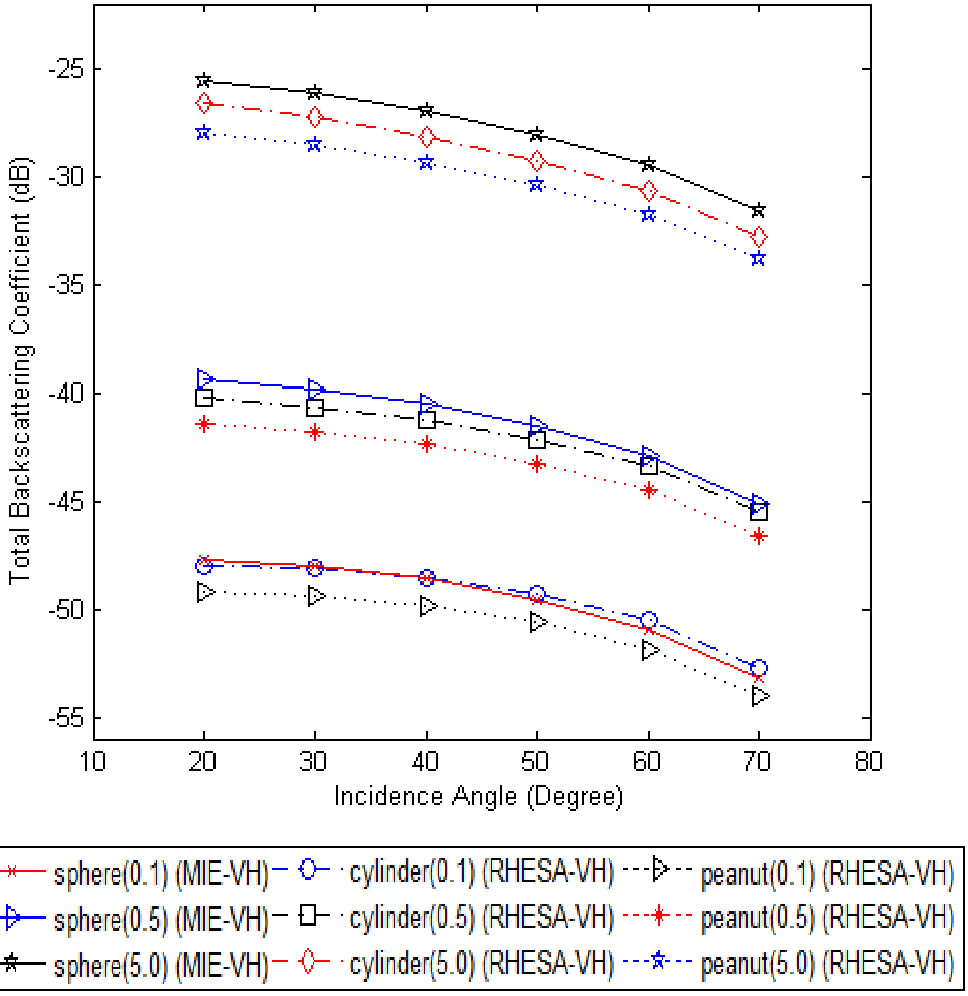

Figure 6.7 Total backscattering comparison between the RT-PACT and RT-RHESA model against 6 different incidence angles with 3 different shapes of scatterers for VH polarization using frequency 15.50GHz and 3 different layer thicknesses (0.1m, 0.5m, 5.0m).

Figure 6.7 shows the comparison of total backscattering between the RT-PACT and RT-RHESA model using 3 different shapes of scatterers which are sphere, cylinder and peanut for VH polarization using the same configuration of parameters and same size of scatterers as Figure 6.6. As noticed from the results, the peanut shape has the lowest total backscattering for all the 3 different layer thicknesses as compared to others.

6.4 Effect of Volume Fraction for Different Shapes of Scatterer on Backscattering

Figure 6.8 shows the comparison of total backscattering between the RT-PACT and RT-RHESA model using 3 different shapes of scatterers which are sphere, cylinder and peanut for VV and HH polarizations. The parameters used for this simulation is stated in Table 6.2. The results are simulated using 3 different volume fractions which are 20%, 30% and 40%. The frequency used is 15.50GHz. The results for sphere shape are simulated using the RT-PACT model while the results for cylinder and peanut shapes are simulated using the RT-RHESA model. There are total 6 incidence angles selected for the simulations. The sizes of the scatterers for the 3 selected shapes are the same as in previous Figure 6.2.

From the results, there are significant differences for the scattering patterns shown by the cylinder shape. As the volume fraction increases, the separation between VV and HH polarizations become bigger when the incidence angles are between 30° to 60° and HH is higher than VV. This is because the surface-volume interactions become more important.

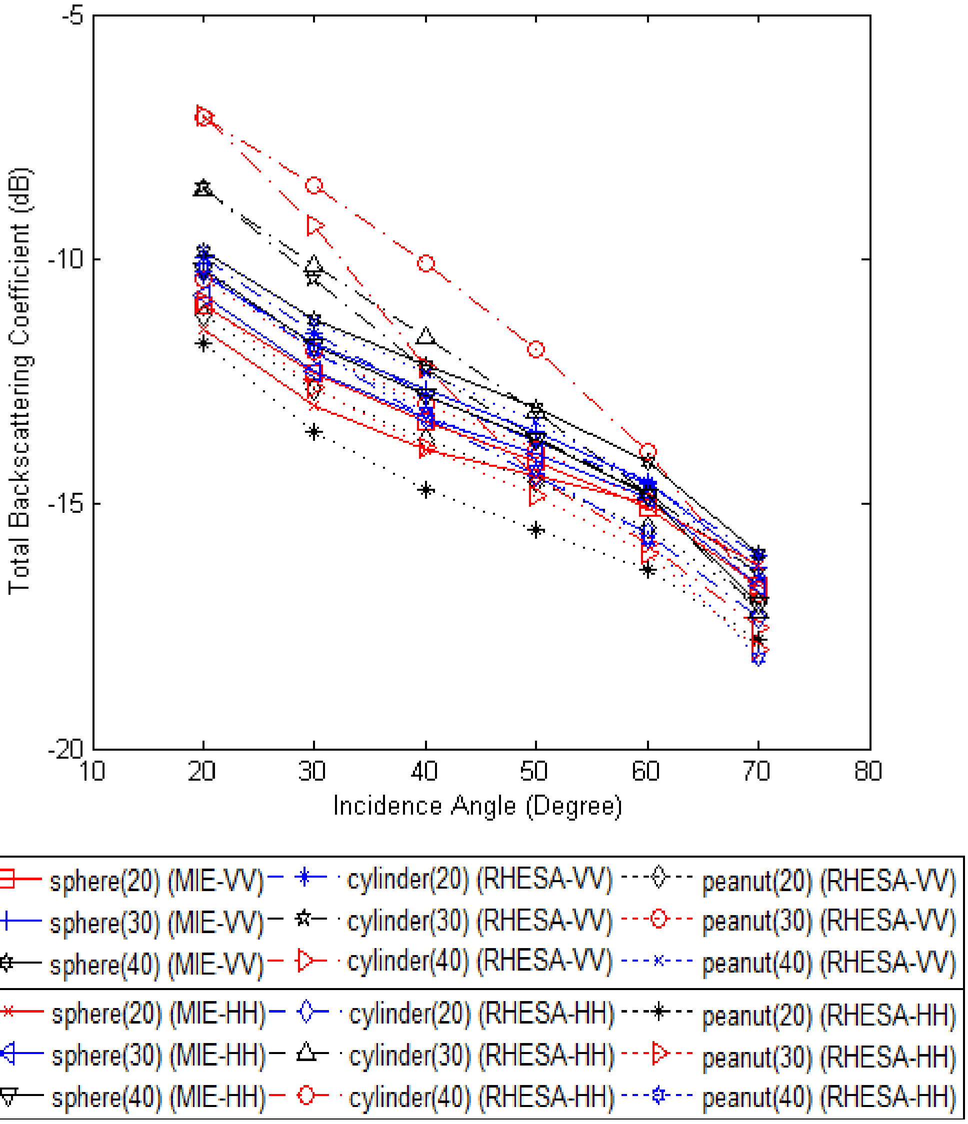

Figure 6.8 Total backscattering comparison between the RT-PACT and RT-RHESA model against 6 different incidence angles with 3 different shapes of scatterers for VV and HH polarizations using frequency 15.50GHz and 3 different volume fractions (20%, 30%, 40%).

Figure 6.9 shows the comparison of total backscattering between the RT-PACT and RT-RHESA model using 3 different shapes of scatterers which are sphere, cylinder and peanut for VH polarization using the same configuration of parameters and same size of scatterers as in Figure 6.8.

In general, the results show that with higher volume fraction, total backscattering for VH for all the 3 shapes of scatterers has increased.

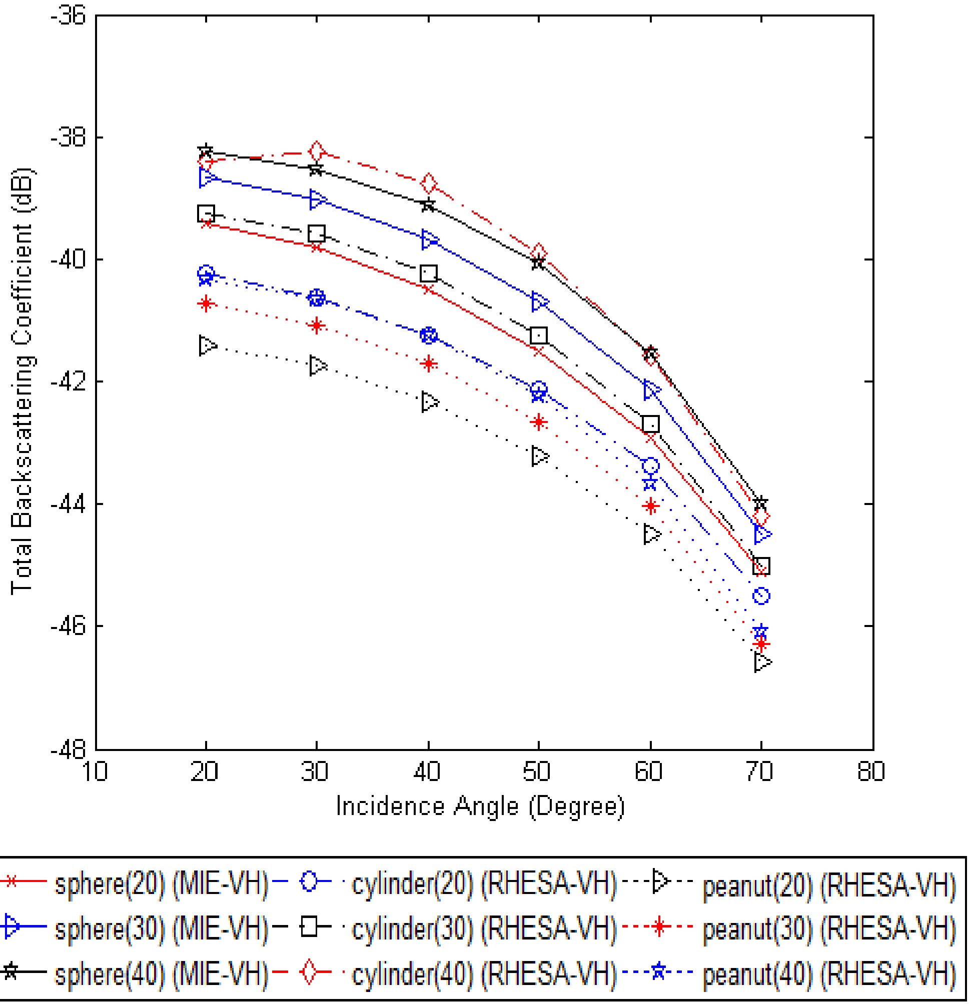

Figure 6.9 Total backscattering comparison between the RT-PACT and RT-RHESA model against 6 different incidence angles with 3 different shapes of scatterers for VH polarization using frequency 15.50GHz and 3 different volume fractions (20%, 30%, 40%).

6.5 Summary

In this chapter, theoretical analysis for the effect of shape of scatterer, effect of frequency, effect of layer thickness and effect of volume fraction on total backscattering are performed using the RT-RHESA model. We will demonstrate the applications of the RT-RHESA model in the later chapter to compare with some ground truth measurement data. This is to further validate the accuracy and the effect of shape of scatterer in contributions to total backscattering. With this, we can have a better understanding of the scattering mechanisms that involve the non-spherical scatterers for a layer of snow.

CHAPTER 7

APPLICATION OF RT-RHESA MODEL

7.1 Introduction

In this chapter, the RT-RHESA model will be further validated with several ground truth measurement data. The shapes selected to compare with the ground truth measurement results are sphere, cylinder and peanut shapes. The ground truth measurement data for dry snow from 2002 to 2004 were collected by RADARSAT satellite that operates at 5.30GHz frequency (C-band) from ice shelf areas (Albert et al., 2012) near Scott Base, Ross Island in Antarctica. Another ground truth measurement data for experiment data measurement were collected from the field measurement program undertaken by NASA’s Cold Land Processes Field Experiment (CLPX) from 2002 to 2003 (Hardy, 2003; Sarabandi, 2003; Yueh et al., 2009). 4 Intensive Observation Periods (IOPs) have been conducted by CLPX during winter of 2002 and the spring of 2003. In February 2002 and February 2003, two of the four IOPs which are IOP1 and IOP3 were carried out. In March 2002 and March 2003, IOP2 and IOP4 were carried out. In order to maintain the consistency, all the four IOPs were conducted on the same day-of-year (DOY) schedule. There were snow pits activities conducted during the IOPs within three larger-scale areas in northern Colorado which are Fraser, North Park, and Rabbit Ears Meso-cell Study Areas (MSAs). A total of three 1 km × 1 km Intensive Study Areas

(ISAs) were located within these three larger-scale areas. The Potter Creek, Illinois River and Michigan River ISAs are located inside the North Park MSA. The Spring Creek, Buffalo Pass and Walton Creek ISAs are located inside the Rabbit Ears MSA. Lastly, the St. Louis Creek, Fool Creek and Alpine ISAs are located inside the Fraser MSA. Each ISA was divided into 4 sectors (Alpha, Beta, Charlie, and Delta) and there were 4 snow pit measurements conducted within each sector. There was the smallest study site (0.8 ha) located within the Fraser MSA called Local Scale Observation Site (LSOS). It was the most intensively measured site. Figure 7.1 shows the locations of the three major MSAs, nine ISAs and one LSOS areas.

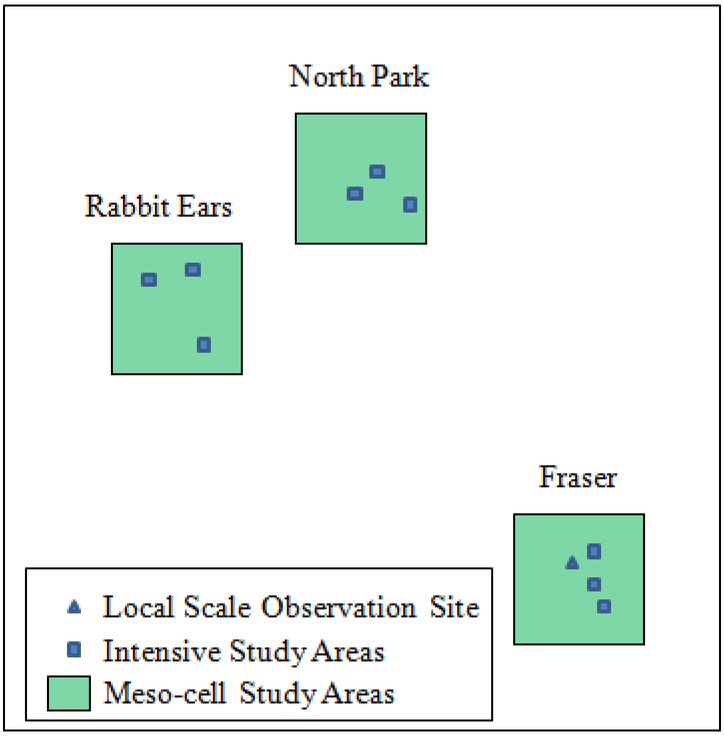

Figure 7.1 Locations of the three major MSAs, nine ISAs and one LSOS areas.

A scatterometer that operated at two frequencies which are L-band (1.1 – 1.4GHz) and Ku-band (15.25 – 15.75GHz) was set up by a team from The University of Michigan to monitor the large clearing areas in LSOS. It was a radar system which could measure amplitude and phase of the backscattered signal. The measurements were taken from three different incidence angles which were 20°, 35°, and 50°. Besides this, there was another measurement set collected by a Ku-band polarimetric scatterometer (POLSCAT) operating at 13.95GHz. It was carried by an aircraft and flew through the three MSAs during the IOPs to generate the normalized radar cross section of the terrain.

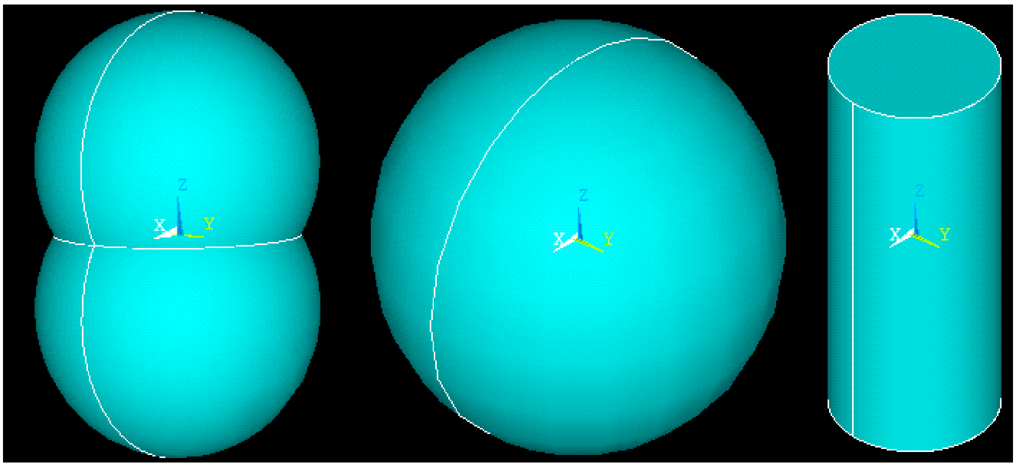

Figure 7.2 Shapes selected for scatterers used in comparison with ground truth measurement data.

Figure 7.2 shows the 3 selected shapes of scatterers used in comparison with ground truth measurement data. The parameters used for the following comparisons of total backscattering coefficient with ground truth measurement data can be found in APPENDIX B.

7.2 Comparison with Measurement Data on Dry Snow

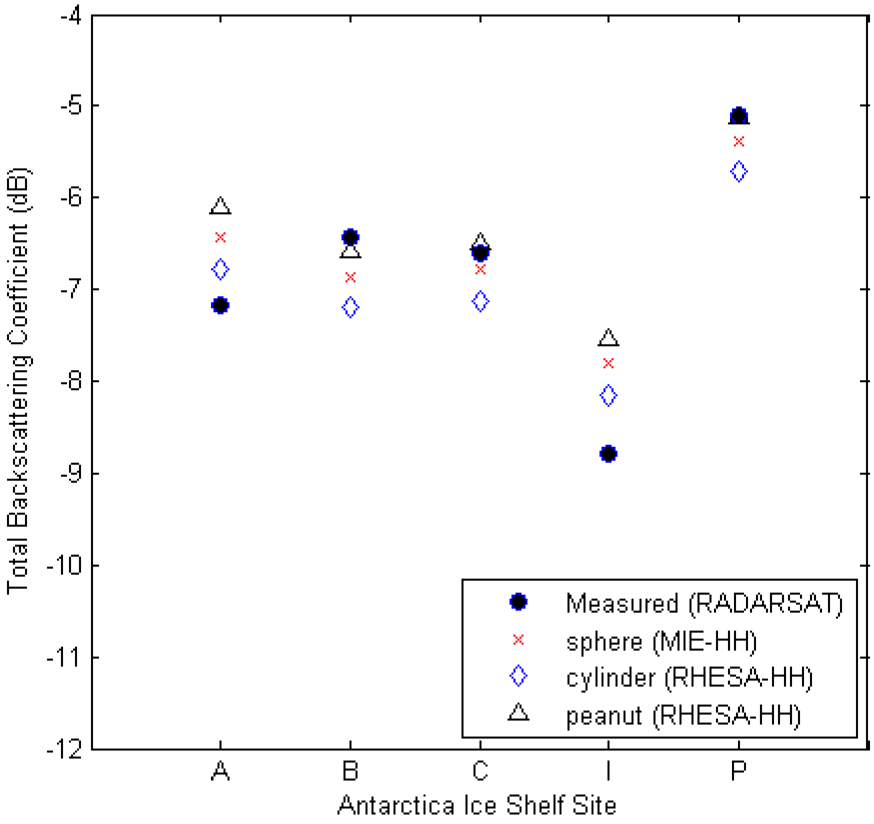

Figure 7.3 Total backscattering comparison between five ice shelf sites A, B, C, I and P in Antarctica between 2002 and 2004 using 3 different shapes of scatterers which are sphere, cylinder and peanut shapes for HH polarization at 30° incidence angle at C-Band.

Figure 7.3 shows the comparison of measurement data collected by RADARSAT satellite from five of the ice shelf sites in Ross Island, Antarctica between 2002 and 2004 with simulation results of the RT-RHESA model using 3 different shapes of scatterers which are sphere, cylinder, and peanut shapes, as shown in Figure 7.2, to examine the effect of different shape of scatterer on total backscattering coefficient. The radius of the sphere shape is

1.1mm and the value is based on the paper in (Albert et al., 2012). The size of the cylinder shape used in the simulation is 1.1mm radius and 1.47mm length. Lastly, the size of the peanut shape is actually a combination of two spherical scatterers of 0.92mm radius each with the combined length of 2.77mm. The volume of the 3 different shapes of scatterers was kept as close as each other. Within the medium, the randomly distributed scatterers are assumed to be identical in size and the orientation of the scatterers are aligned to Z direction (symmetry at Z axis). As shown by the results, we notice that at sites like B, C and P, the total backscattering coefficient from the peanut shape scatterers give better match than that of sphere and cylinder shapes scatterers. While for sites A and I, the cylinder shape scatterers give the closest match as compared to others. The reason for these could be the shape of the simulated scatterers is closer to the real shape of scatterers in those areas.

7.3 Comparison with Measurement Data on Experimental Data Measurement

The following comparisons will use the 3 selected shapes shown in Figure 7.2 to compare with several experimental data measurements collected by the NASA's CLPX. The radius of the sphere shape is 0.54mm which is estimated based on the paper in (Du et al., 2005). The size of the cylinder shape used in the simulation is 0.35mm radius and 1.7mm length and the size of the peanut shape is actually a combination of two spherical scatterers of 0.45 mm radius each with the combined length of 1.36mm. The volume of the 3 different shapes of scatterers was kept as close as each other. Within the medium, the randomly distributed scatterers are assumed to be identical in size and the orientation of the scatterers are aligned to Z direction (symmetry at Z axis).

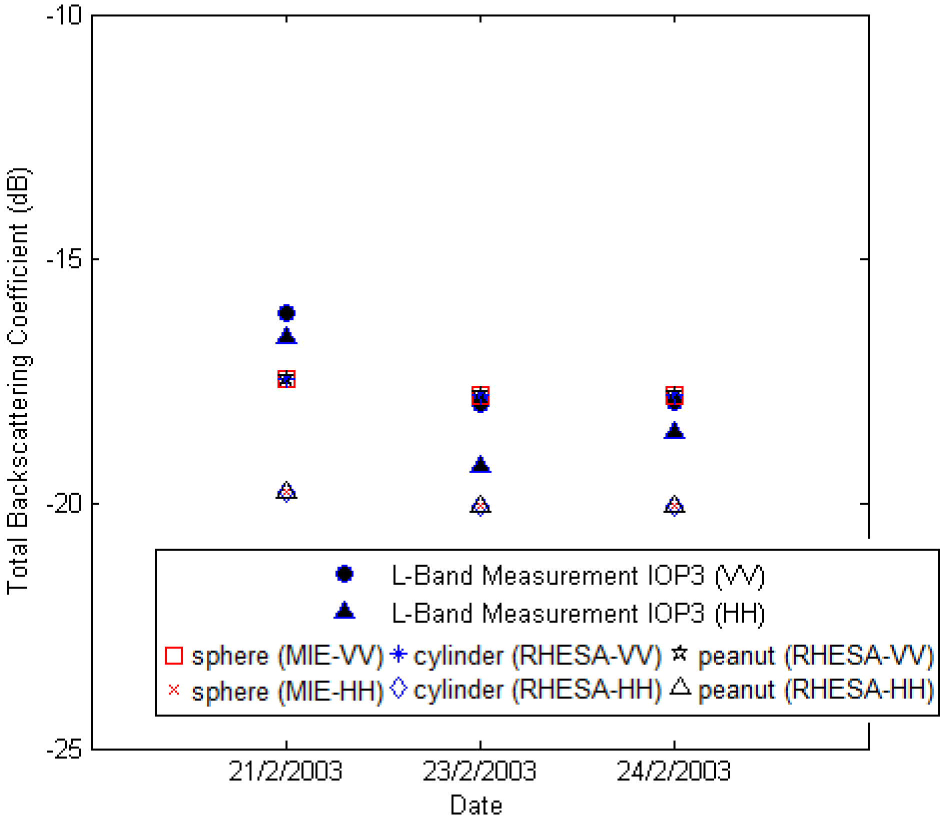

Figure 7.4 Total backscattering comparison between sphere, cylinder and peanut shapes with data collected from CLPX during IOP3 at LSOS for VV and HH polarizations at 35° incidence angle at L-Band.

As shown in Figure 7.4, three experimental data measurements of three different days collected at LSOS during 2003 are selected to compare with the simulation results of the 3 different shapes of scatterers using the RT-RHESA model. The measured data of total backscattering coefficient were collected by a scatterometer operated at L-band frequency. Snow pit data collected during

IOP3 were snow layer thickness, snow surface wetness, snow density, temperature, backscattered coefficient. The parameter for lower half soil permittivity was estimated using the graph from the paper in (Zhang et al., 2003). All measurements from the radar were taken at incidence angle 35°. The results show that the simulated results match the ground truth measurement data well. The scattering patterns between the 3 different shapes of scatterers are quite similar due to a low frequency was used. The wavelength is much bigger as compared to the size of the scatterers.

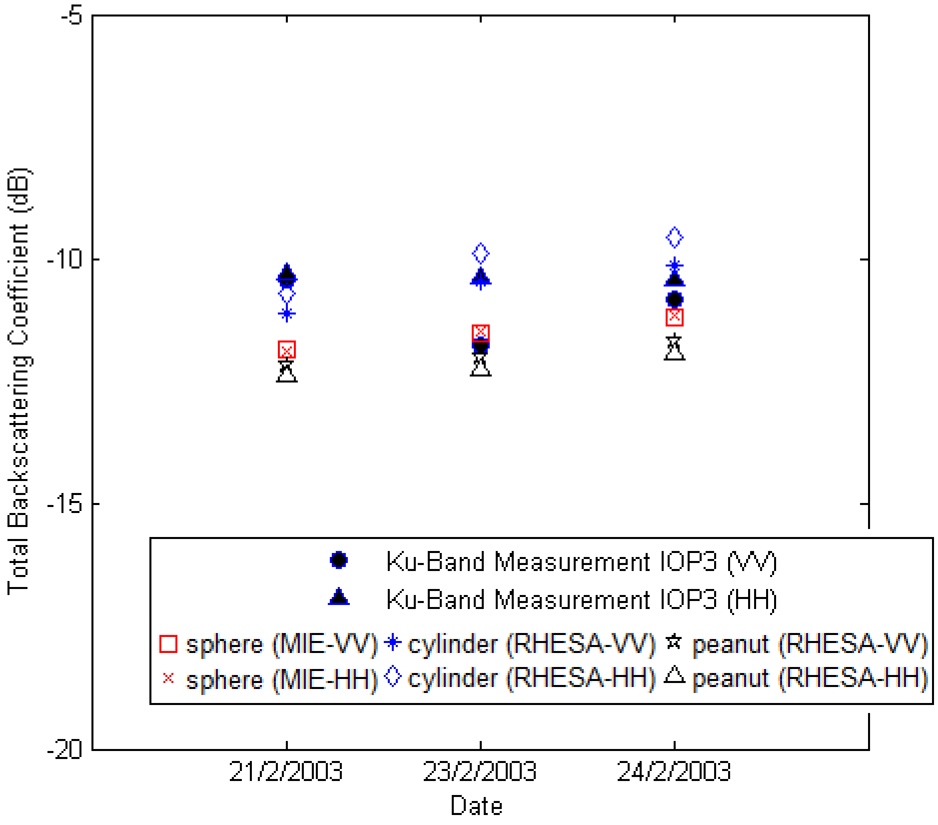

Figure 7.5 Total backscattering comparison between sphere, cylinder and peanut shapes with data collected from CLPX during IOP3 at LSOS for VV and HH polarizations at 35° incidence angle at Ku-Band.

Figure 7.5 shows the comparison of total backscattering coefficient using the same ground truth measurement data as Figure 7.4 but at Ku-band frequency. The simulated results of different shapes of scatterers match the ground truth measurement data well. At higher frequency, different shapes of scatterers reflect more differences among the cylinder, peanut and sphere shapes. The cylinder shape scatterers give better match for HH polarization at Ku-band as compared to others.

As shown in Figure 7.6, four experimental data measurements of two different periods, two from North Park's Illinois River during IOP1 and two from Rabbit Ears's Buffalo Pass and Spring Creek during IOP4 are selected to compare with the simulation results of the 3 different shapes of scatterers using the RT-RHESA model. The POLSCAT scatterometer operated at frequency of 13.95GHz which was carried on board the plane was used to collect the ground truth measurement data from the ISAs located near to the flight lines (< 70m) conducted during these two periods. The cylinder shape gives higher total backscattering coefficient for HH polarization as compared to the sphere and peanut shapes. This is because during IOP4, the volume fraction is higher and the snow layer is thicker as compared with IOP1. The cylinder shape is more sensitive to volume fraction as observed from the theoretical analysis performed in the previous chapter. The results show that the simulated results match the ground truth measurement data especially the sphere and peanut shapes.

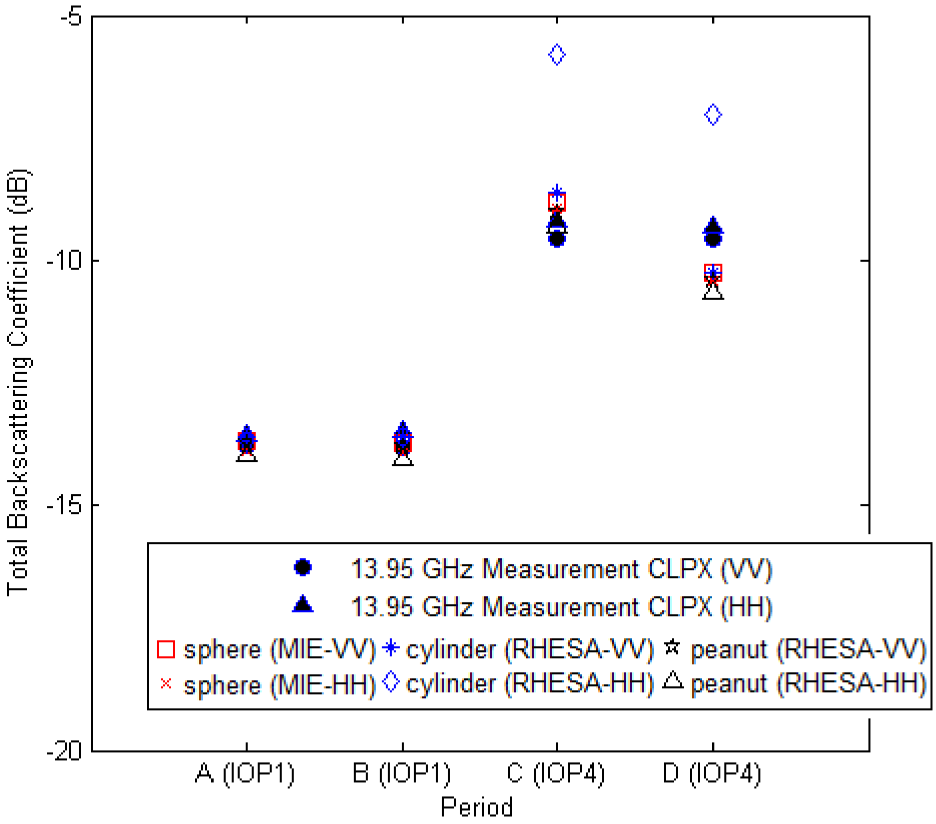

Figure 7.6 Total backscattering comparison between sphere, cylinder and peanut shapes with data collected from CLPX during IOP1 (A, B) on 21/2/2002 and IOP4 (C, D) on 30/3/2003 for VV and HH polarizations at incidence angle 40° at frequency of 13.95GHz.

7.4 Summary

The RT-RHESA model has been used to simulate a layer of snow embedded with non-spherical scatterers and the simulated results are compared with several ground truth measurement data to validate its accuracy and the effect of shape of scatterer on total backscattering coefficient. In some cases, the non-spherical scatterers can have better match as compared to spherical scatterers. This provides a way that different shapes of scatterers could be used to model the contributions to total backscattering coefficient due to the metamorphism and sintering processes. In Chapter 8, we will conclude and summarize the study of this dissertation.

CHAPTER 8

SUMMARY AND CONCLUSION

8.1 Discussion and Conclusion

The study of this dissertation is focused on the development of a new theoretical model based on radiative transfer theory using the numerical computation to solve the wave scattering problems. Using the two numerical methods discussed in Chapter 3 and Chapter 5 which are EPA and RHESA, two new numerical theoretical models named RT-EPA and RT-RHESA models have been developed and studied.

The existing RT-PACT theoretical model that uses analytical solution to compute the total backscattering coefficient of a layer of snow has its limitation of scattering from basic shape of scatterers to be applied in the further study of microwave interactions with other mediums where scatterers are irregular shape. Due to the complexity of some scatterer shapes, it is difficult for analytical solution to derive and formulate scattering from these shapes mathematically. To continue to expand the current backscatter model using analytical solution is getting difficult as every time when there is a new shape to be added in, formulation for the new added shape will have to be re-derived and re-formulated. This is a very time-consuming process. Besides this, a basic shape like sphere is too basic in modeling the complex natural mediums in microwave remote sensing field. Thus, a new theoretical model can be a good solution and tool to help to find out the answer.

Two of the numerical methods discussed in Chapter 3 and Chapter 5 such as EPA and RHESA have been incorporated into the existing RT-PACT model and tested with several different shapes of scatterers like sphere, cylinder and peanut shapes.

Theoretical analysis is performed using the RT-EPA and RT-RHESA models in Chapter 4 and Chapter 6. Chapter 4 compares the RT-EPA and RT-PACT models using different frequencies, different incidence angles and different spherical scatterer radius sizes to do theoretical analysis and study the computational performance of the RT-EPA model.

Results computed by the RT-EPA model matched well with the RT-PACT model. At frequency 1.25GHz, the element edge length size used is 0.26mm, where the wavelength is much larger compared to the element edge length size, the accuracy of the RT-EPA model is less as compared to the RT-PACT model. As frequency increases, the accuracy of the RT-RHESA model is improved. When there are more SWG elements used to mesh the volume of the scatterer, the computational time of the RT-RHESA model is also increased.

Chapter 6 compares the RT-RHESA and RT-PACT models using different frequencies, different layer thicknesses, and different volume fractions with different shapes of scatterers such as cylinder and peanut shapes to examine the performance of the RT-RHESA model in computing the scattering of different shapes of scatterers and to find out the possible scattering pattern which could be produced by these shapes of scatterers.

The results computed by the RT-RHESA model shows there are noticeable difference between each shape of scatterer that is simulated. The shape of scatterer is found to be important when the frequency is high as the wavelength becomes comparable to the size of the scatterer. The cylinder shape gives more separation between HH and VV as the volume fraction increases. Thus, the cylinder shape is found to be more sensitive to volume fraction compared to the sphere and peanut shapes.

A further validation of the accuracy of the RT-RHESA model and the effect of shape of scatterer in contributions to total backscattering coefficient with real data is presented in Chapter 7, the results simulated by the RT-RHESA model are compared with some of the ground truth measurement data. Due to the metamorphism and sintering processes, the shape of scatterer may changes from time to time. By using the RT-RHESA model, a better representation of the shape of scatterer embedded inside a medium could provide a better understanding of the interactions between the microwave and the medium. The shape of scatterer plays an important role in contributions to total backscattering coefficient especially when the frequency is high enough as the wavelength is comparable to the size of the scatterers.

A new RT theoretical model that incorporates the RHESA model to give the capability to simulate arbitrary shape of scatterers has been developed and studied. Theoretical analysis using different frequencies, incidence angles, layer thicknesses and volume fractions are performed and good matching of results among the RT-PACT and the RT-RHESA are obtained. Comparisons of ground truth measurement data with the RT-RHESA model are performed. The results show that in some cases, non-spherical scatterers can have better match as compared to spherical scatterers. With the new developed RT-RHESA theoretical model, this could provides a base for future researchers to works on different kind of medium where the shape of the scatterer is irregular.

8.2 Limitation and Future Improvement

The RT-RHESA model is using a simplified phase matrix which assumes the scatterers are identical in size and orientation angle where the orientation of the scatterers are aligned to *Z* direction. The shape of the scatterer is assumed to have at least a plane of symmetry (symmetry at *Z* axis). This allows the medium to be considered as a macroscopically isotropic and mirror-symmetric scattering medium (ISM) and the phase matrix is independent of the azimuthal scattering angles. This allows faster computational time to be achieved by reducing the total scattered angles of different orientation angles. However, this also limited the RT-RHESA model to be applied for scatterer which shape does not have a plane of symmetry where more computation time will be needed.

Future works can also include extension of this model to more complex shapes so that vegetation medium with leaves of various shapes, branches and trunks can be modeled. For further improvement of computational speed in numerical calculations can be studied so that this model can be applied for wider range of medium that may contain many types of scatterers with different shapes, sizes, orientations and distributions.

REFERENCES

Albert, M.D., Lee, Y.J., Ewe, H.T. and Chuah, H.T., 2012. Multilayer Model Formulation and Analysis of Radar Backscattering from Sea Ice. *Progress in Electromagnetics Research-Pier*, 128(February), pp.267–290.

Ao, C.O., 2001. *Electromagnetic Wave Scattering by Discrete Random Media with Remote Sensing Applications*. University of California, Berkeley.

Beckmann, P. and Spizzichino, A., 1987. *The Scattering of Electromagnetic Waves from Rough Surfaces*, Artech House.

Besic, N. et al., 2012. Dry snow backscattering sensitivity on density change for SWE estimation. *2012 IEEE International Geoscience and Remote Sensing Symposium*. July 2012 IEEE, pp. 4418–4421.

Bohren, C.F. and Huffman, D.R., 1983. *Absorption and scattering of light by small particles*, Wiley.

Chandrasekhar, S., 1960. *Radiative Transfer*, New York: Dover.

Chen, K.S. and Fung, A.K., 2003. Emission of rough surfaces calculated by the integral equation method with comparison to three-dimensional moment method simulations. *IEEE Transactions on Geoscience and Remote Sensing*, 41(1), pp.90–101.

Chenga Lu, C.C. and Chew, W.C., 1995. The Use of Huygens' Equivalence Principle for Solving 3-D Volume Integral Equation of Scattering. *IEEE Transactions on Antennas and Propagation*, 43(5), pp.500–507.

Chuah, H.-T., Tjuatja, S., Fung, A.K. and Bredow, J.W., 1997. Radar backscatter from a dense discrete random medium. *IEEE Transactions on Geoscience and Remote Sensing*, 35(4), pp.892–900.

Chuah, H.T., Tjuatja, S., Fung, A.K. and Bredow, J.W., 1996. A Phase matrix for a dense discrete random medium: Evaluation of volume scattering coefficient. *IEEE Transactions on Geoscience and Remote Sensing*, 34(5), pp.1137–1143.

Colbeck, S.C., 1997. A review of sintering in seasonal snow. *CRREL Report*, (97–10), p.12.

Colbeck, S.C., 1982. An overview of seasonal snow metamorphism. *Reviews of Geophysics*, 20(1), pp.45–61.

Du, J., Shi, J. and Wu, S., 2005. A comparison of a second-order snow model with field observations. *International Geoscience and Remote Sensing Symposium (IGARSS)*. 2005 pp. 2649–2651.

Eom, H.J. and Fung, A.K., 1984. A scatter model for vegetation up to Ku-band. *Remote Sensing of Environment*, 15(3), pp.185–200.

Ewe, H.T. and Chuah, H.T., 1999. A microwave scattering model for an electrically dense vegetation medium. *Geoscience and Remote Sensing Symposium, 1999. IGARSS '99 Proceedings. IEEE 1999 International*. 1999 pp. 2428–2430 vol.5.

Ewe, H.T. and Chuah, H.T., 1998. An analysis of the scattering of discrete scatterers in an electrically dense medium. *IGARSS '98 - 1998 International Geoscience and Remote Sensing Symposium, Proceedings Vols 1-5: Sensing and Managing the Environment*. 1998 pp. 2378–2380.

Ewe, H.T. and Chuah, H.T., 2000. Electromagnetic scattering from an electrically dense vegetation medium. *IEEE Transactions on Geoscience and Remote Sensing*, 38(5 I), pp.2093–2105.

Fu, X., Jiang, L. and Ewe, H.T., 2016a. A novel relaxed hierarchical equivalent source algorithm (RHESA) for electromagnetiFu, X., Jiang, L.-J. and Ewe, H.T., 2016. A novel relaxed hierarchical equivalent source algorithm (RHESA) for electromagnetic scattering analysis of dielectric objects. *Journal of Electromagnetic Waves and Applications*, 30(12), pp.1631–1642.

Fu, X., Jiang, L. and Ma, Z.H., 2015. Accuracy enhancement of the equivalence principle algorithm based on the meshless spherical surface. *ICCEM 2015 - 2015 IEEE International Conference on Computational Electromagnetics*, pp.135–137.

Fu, X., Jiang, L.J., Ma, Z.H. and He, S.Q., 2016b. Performance Enhancement of Equivalence Principle Algorithm. *IEEE Antennas and Wireless Propagation Letters*, 15, pp.480–483.

Fung, A.K., 1968. Mechanisms of polarized and depolarized scattering from a rough dielectric surface. *Journal of the Franklin Institute*, 285(2), pp.125–133.

Fung, A.K., 1994. *Microwave Scattering and Emission Models and Their Applications*, Artech House.

Fung, A.K., 1967. Theory of cross polarized power returned from a random surface. *Applied Scientific Research*, 18(1), pp.50–60.

Fung, A.K. and Chen, K.S., 2004. An update on the IEM surface backscattering model. *IEEE Geoscience and Remote Sensing Letters*, 1(2), pp.75–77.

Fung, A.K. and Eom, H.J., 1985. A Study of Backscattering and Emission from Closely Packed Inhomogeneous Media. *IEEE Transactions on Geoscience and Remote Sensing*, GE-23(5), pp.761–767.

Fung, A.K., Nesti, G., Sieber, A.J. and Coppo, P., 1997. A further study of the IEM surface scattering model. *IEEE Transactions on Geoscience and Remote Sensing*, 35(4), pp.901–909.

Gherboudj, I., Bernier, M., Hicks, F. and Leconte, R., 2007. Physical characterization of air inclusions in river ice. *Cold Regions Science and Technology*, 49(3), pp.179–194.

Gibson, W.C., 2007. *The Method of Moments in Electromagnetics*, CRC Press.

Hardy, J., 2003. *CLPX-Ground: Snow Measurements at the Local Scale Observation Site (LSOS), Version 1*. IOP3. Boulder, Colorado USA: NSIDC DAAC.

Harrington, R.F., 1987. The Method of Moments in Electromagnetics. *Journal of Electromagnetic Waves and Applications*, 1(3), pp.181–200.

Jin, J.M., 2015. *The Finite Element Method in Electromagnetics*, Wiley.

Jin, Y.Q., 1993. *Electromagnetic Scattering Modelling for Quantitative Remote Sensing*, World Scientific.

Karam, M.A. and Fung, A.K., 1988. Electromagnetic scattering from a layer of finite length, randomly oriented, dielectric, circular cylinders over a rough interface with application to vegetation. *International Journal of Remote Sensing*, 9(6), pp.1109–1134.

Karam, M.A., Fung, A.K., Lang, R.H. and Chauhan, N.S., 1992. A microwave scattering model for layered vegetation. *IEEE Transactions on Geoscience and Remote Sensing*, 30(4), pp.767–784.

Karam, M. a, Amur, F., Fung, A.K. and Box, U.T. a, 1993. Electromagnetic Wave Scattering From a Forest or Vegetation Canopy : Ongoing Research at the University of Texas at Arlington. *IEEE Antennas and Propagation Magazine*, 35(2), pp.18–25.

Kokhanovsky, A.A., 2004. *Light Scattering Media Optics*, Springer.

Kokhanovsky, A.A., 2013. *Light Scattering Reviews 8: Radiative transfer and light scattering*, Springer Berlin Heidelberg.

Kovvali, N., 2011. *Theory and Applications of Gaussian Quadrature Methods*, Morgan & Claypool.

Leader, J.C., 1978. Incoherent backscatter from rough surfaces: The two-scale model reexamined. *Radio Science*, 13(3), pp.441–457.

Lee, Y.J., Lim, W.K. and Ewe, H.-T., 2011. A STUDY OF AN INVERSION MODEL FOR SEA ICE THICKNESS RETRIEVAL IN ROSS ISLAND, ANTARCTICA. *Progress In Electromagnetics Research*.

Li, M., Francavilla, M.A., Chen, R. and Vecchi, G., 2017. Nested Equivalent Source Approximation for the Modeling of Penetrable Bodies. *IEEE Transactions on Antennas and Propagation*, 65(2), pp.954–959.

Li, M.K. and Chew, W.C., 2007. Wave-field interaction with complex structures using equivalence principle algorithm. *IEEE Transactions on Antennas and Propagation*, 55(1), pp.130–138.

Liou, K.N., Yang, P. and Takano, Y., 2016. *Light Scattering by Ice Crystals: Fundamentals and Applications*, Cambridge University Press.

Liu, P. and Jin, Y.Q., 2004. The finite-element method with domain decomposition for electromagnetic bistatic scattering from the comprehensive model of a ship on and a target above a large-scale rough sea surface. *IEEE Transactions on Geoscience and Remote Sensing*, 42(5), pp.950–956.

Lu, C.-C. and Chew, W.C., 1994. A multilevel algorithm for solving a boundary integral equation of wave scattering. *Microwave and Optical Technology Letters*, 7(1), p.1994.

Lu, Y.L.Y. and Shen, C.Y., 1997. A domain decomposition finite-difference method for parallel numerical implementation of time-dependent Maxwell's equations. *IEEE Transactions on Antennas and Propagation*, 45(3), pp.556–562.

Ma, Z.H., Jiang, L., Qian, Z.G. and Chew, W.C., 2011. A low frequency stable EPA method accelerated by the adaptive cross approximation algorithm. *IEEE Antennas and Propagation Society, AP-S International Symposium (Digest)*. 2011 pp. 2704–2707.

Mishchenko, M.I., Hovenier, J.W. and Travis, L.D., 2000. Light Scattering by Nonspherical Particles: Theory, Measurements, and Applications. *Measurement Science and Technology*, 11(12), p.1827.

Mishchenko, M.I., Travis, L.D. and Lacis, A.A., 2006. *Multiple Scattering of Light by Particles: Radiative Transfer and Coherent Backscattering*, Cambridge University Press.

Mishchenko, M.I., Travis, L.D. and Lacis, A.A., 2002. *Scattering, Absorption, and Emission of Light by Small Particles*, Cambridge University Press.

Rao, S.M., Wilton, D.R. and Glisson, A.W., 1982. Electromagnetic Scattering by Surfaces of Arbitrary Shape. *IEEE Transactions on Antennas and Propagation*, 30(3), pp.409–418.

Rees, W.G., 2005. *Remote Sensing of Snow and Ice*, CRC Press.

Ruck, G.T., Barrick, D.E. and Stuart, W.D., 2002. *Radar Cross Section Handbook*, Peninsula Publishing.

Sarabandi, K., 2003. *CLPX-Ground: Ground-based L and Ku band polarimetric scatterometry, Version 1*. IOP3. Boulder, Colorado USA: NSIDC DAAC.

Schaubert, D.H. et al., 1984. A Tetrahedral Modeling Method for Electromagnetic Scattering by Arbitrarily Shaped Inhomogeneous Dielectric Bodies. *IEEE Transactions on Antennas and Propagation*, 32(1), pp.77–85.

Shin, R.T. and Kong, J.A., 1989. Radiative transfer theory for active remote sensing of two-layer random media. *Progress in Electromagnetics Research-Pier*, 1, pp.359–417.

Stratton, J. and Chu, L., 1939. Diffraction Theory of Electromagnetic Waves. *Physical Review*, 56(1), pp.99–107.

Syahali, S. and Ewe, H.T., 2013. Remote sensing backscattering model for sea ice: Theoretical modelling and analysis. *Advances in Polar Science*, 24(4), pp.248–257.

Taflove, A. and Hagness, S.C., 2005. *Computational Electrodynamics: The Finite-Difference Time-Domain Method, Third Edition*, Artech House.

Tiryaki, B., 2010. *Solution of electromagnetics problems with the equivalence principle algorithm*. Master thesis, Bilkent University.

Tjuatja, S., Fung, A.K. and Bredow, J., 1992. Scattering Model for Snow-Covered Sea Ice. *IEEE Transactions on Geoscience and Remote Sensing*, 30(4), pp.804–810.

Tsang, L., Ding, K.-H., Huang, S. and Xu, X., 2013. Electromagnetic Computation in Scattering of Electromagnetic Waves by Random Rough Surface and Dense Media in Microwave Remote Sensing of Land Surfaces. *Proceedings of the IEEE*, 101(2), pp.255–279.

Tsang, L. and Ishimaru, A., 1987. Radiative Wave Equations for Vector Electromagnetic Propagation in Dense Nontenuous Media. *Journal of Electromagnetic Waves and Applications*, 1(1), pp.59–72.

Tsang, L., Kong, J.A. and Shin, R.T., 1985. Theory of microwave remote sensing. *A WileyInterscience publication*, pp.214–235.

Tsang, L., Kubacsi, M.C. and Kong, J.A., 1981. Radiative transfer theory for active remote sensing of a layer of small ellipsoidal scatterers. *Radio Science*, 16(3), pp.321–329.

Tzeng, Y.C., Tjuatja, S. and Fung, A.K., 1992. A T-matrix Approach To Scattering From A Snow Layer. *[Proceedings] IGARSS '92 International Geoscience and Remote Sensing Symposium*. 1992 IEEE, pp. 828–829.

Ulaby, F.T., Moore, R.K. and Fung, A.K., 1986. *Microwave remote sensing: Active and passive. Volume 3 - From theory to applications*, Artech House; Remote Sensing Series, 4.

Valenzuela, G., 1967. Depolarization of EM waves by slightly rough surfaces. *IEEE Transactions on Antennas and Propagation*, 15(4), pp.552–557.

Van De Hulst, H.C., 1981. *Light scattering by small particles*, Dover Publications.

Wait, J.R., 1959. *Electromagnetic radiation from cylindrical structures,* Pergamon Press, New York.

Wait, J.R., 1955. Scattering of a Plane Wave From a Circular Dielectric Cylinder At Oblique Incidence. *Canadian Journal of Physics*, 33(5), pp.189–195.

Wu, T.D. and Chen, K.S., 2004. A reappraisal of the validity of the IEM model for backscattering from rough surfaces. *IEEE Transactions on Geoscience and Remote Sensing*. 2004 pp. 743–753.

Yueh, S.H. et al., 2009. Airborne Ku-band polarimetric radar remote sensing of terrestrial snow cover. *IEEE Transactions on Geoscience and Remote Sensing*, 47(10), pp.3347–3364.

Zhang, Z., Shi, J., Zhang, Z. and Zhao, K., 2003. The estimation of dielectric constant of frozen soil-water mixture at microwave bands. *IGARSS 2003. 2003 IEEE International Geoscience and Remote Sensing Symposium. Proceedings (IEEE Cat. No.03CH37477)*, 4(40271080), pp.2903–2905.

APPENDIX A

The 4 × 4 phase matrix:

$$P = 4\pi \langle M \rangle / (A \cos \theta_s)$$

where θ_s is the angle between the scattered direction and direction normal to illuminated area A and the Stokes matrix M is given as (Fung, 1994):

$$\begin{bmatrix} |S_{vv}|^2 & |S_{vh}|^2 & Re(S_{vv}S_{vh}^*) & -Im(S_{vv}S_{vh}^*) \\ |S_{hv}|^2 & |S_{hh}|^2 & Re(S_{hv}S_{hh}^*) & -Im(S_{hv}S_{hh}^*) \\ 2Re(S_{vv}S_{hv}^*) & 2Re(S_{vh}S_{hh}^*) & Re(S_{vv}S_{hh}^*+S_{vh}S_{hv}^*) & -Im(S_{vv}S_{hh}^*-S_{vh}S_{hv}^*) \\ 2Im(S_{vv}S_{hv}^*) & 2Im(S_{vh}S_{hh}^*) & Im(S_{vv}S_{hh}^*+S_{vh}S_{hv}^*) & Re(S_{vv}S_{hh}^*-S_{vh}S_{hv}^*) \end{bmatrix}$$

The 2 × 2 amplitude scattering matrix (Fung, 1994):

$$\begin{bmatrix} E_v^s \\ E_h^s \end{bmatrix} = \frac{e^{jkR}}{R} \begin{bmatrix} S_{vv} & S_{vh} \\ S_{hv} & S_{hh} \end{bmatrix} \begin{bmatrix} E_v^i \\ E_n^i \end{bmatrix}$$

where S_{pq} ($pg = v, h$) is the scattering amplitude in meters and R is the distance from the center of the illuminated area to the observation point.

The rotation angles *α*, *β* and *γ* of a scatterer

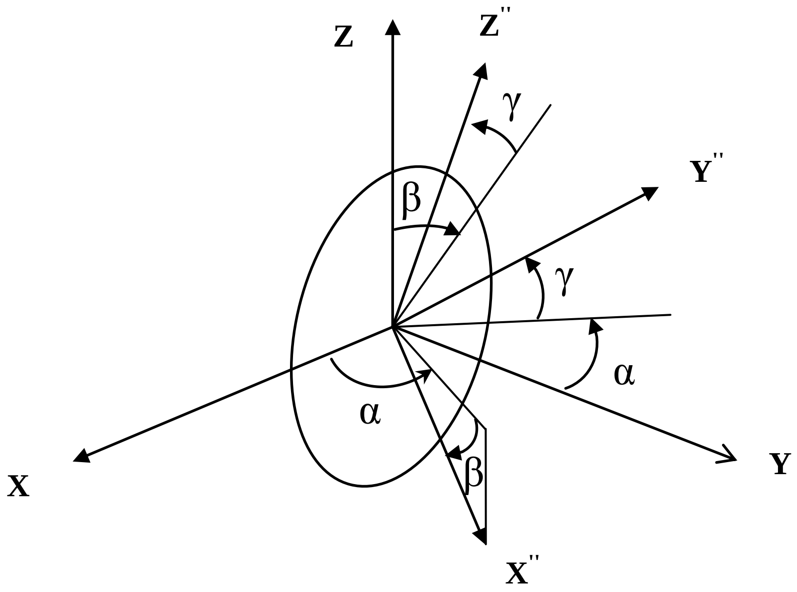

APPENDIX B

Parameters used in Figure 7.3:

Sites **Parameters**	A	B	C	I	P
Layer Thickness (m)	250^*	250^*	250^*	250^*	250^*
Volume Fraction of Scatterer (%)	32^+	32^+	32^+	32^+	32^+
Relative Permittivity of Scatterer	(1.58, 7.39E-05)	(1.50, 6.72E-05)	(1.53, 7.14E-05)	(1.42 4.76E-05)	(1.57, 4.74E-05)
Relative Permittivity of Top Layer	(1.0, 0.0)$^+$	(1.0, 0.0)$^+$	(1.0, 0.0)$^+$	(1.0, 0.0)$^+$	(1.0, 0.0)$^+$
Background Relative Permittivity	(1.0, 0.0)$^+$	(1.0, 0.0)$^+$	(1.0, 0.0)$^+$	(1.0, 0.0)$^+$	(1.0, 0.0)$^+$
Relative Permittivity of Bottom Layer	(59.0, 42.0)$^+$	(59.0, 42.0)$^+$	(59.0, 42.0)$^+$	(59.0, 42.0)$^+$	(59.0, 42.0)$^+$
Top Surface RMS Height, Correlation Length	0.39cm, 2.1cm	0.51cm, 3.17cm	0.13cm, 4.88cm	0.14cm, 34.00cm	0.30cm, 14.77cm
Bottom Surface RMS Height, Correlation Length	0.58cm*, 4.70cm*	0.58cm*, 4.70cm*	0.58cm*, 4.70cm*	0.42cm*, 4.70cm*	0.58cm*, 4.70cm*

Parameters used in Figure 7.4:

Dates Parameters	21/2/2003	23/2/2003	24/2/2003
Layer Thickness (m)	0.62	0.99	1.08
Volume Fraction of Scatterer (%)	23^{+}	23^{+}	23^{+}
Relative Permittivity of Scatterer	(3.15, 0.001)*	(3.15, 0.001)*	(3.15, 0.001)*
Relative Permittivity of Top Layer	(1.0, 0.0)$^{+}$	(1.0, 0.0)$^{+}$	(1.0, 0.0)$^{+}$
Background Relative Permittivity	(1.0, 0.0)*	(1.0, 0.0)*	(1.0, 0.0)*
Relative Permittivity of Bottom Layer	(6.0, 0.0)*	(6.0, 0.0)*	(6.0, 0.0)*
Top Surface RMS Height, Correlation Length	0.8cm*, 6.0cm*	0.6cm*, 10.0cm*	0.6cm*, 10.0cm*
Bottom Surface RMS Height, Correlation Length	0.68cm*, 6.0cm*	0.75cm*, 10.0cm*	0.75cm*, 10.0cm*

Parameters used in Figure 7.5:

Dates **Parameters**	21/2/2003	23/2/2003	24/2/2003
Layer Thickness (m)	0.62	0.99	1.08
Volume Fraction of Scatterer (%)	23^{+}	23^{+}	23^{+}
Relative Permittivity of Scatterer	(3.15, 0.001) *	(3.15, 0.001) *	(3.15, 0.001) *
Relative Permittivity of Top Layer	(1.0, 0.0) $^{+}$	(1.0, 0.0) $^{+}$	(1.0, 0.0) $^{+}$
Background Relative Permittivity	(1.0, 0.0) *	(1.0, 0.0) *	(1.0, 0.0) *
Relative Permittivity of Bottom Layer	(6.0, 0.0) *	(6.0, 0.0) *	(6.0, 0.0) *
Top Surface RMS Height, Correlation Length	0.8cm*, 6.0cm*	0.6cm*, 10.0cm*	0.6cm*, 10.0cm*
Bottom Surface RMS Height, Correlation Length	0.68cm*, 6.0cm*	0.75cm*, 10.0cm*	0.75cm*, 10.0cm*

Parameters used in Figure 7.6:

Periods / **Parameters**	IOP1 A	IOP1 B	IOP4 C	IOP4 D
Layer Thickness (m)	0.10	0.17	3.30	2.13
Volume Fraction of Scatterer (%)	26+	24+	36+	38+
Relative Permittivity of Scatterer	(3.15, 0.001) *	(3.15, 0.001) *	(3.15, 0.001) *	(3.15, 0.001) *
Relative Permittivity of Top Layer	(1.0, 0.0) +	(1.0, 0.0) +	(1.0, 0.0) +	(1.0, 0.0) +
Background Relative Permittivity	(1.0, 0.0) *	(1.0, 0.0) *	(1.0, 0.0) *	(1.0, 0.0) *
Relative Permittivity of Bottom Layer	(6.0, 0.0) *	(5.2, 0.0) *	(6.0, 0.0) *	(6.0, 0.0) *
Top Surface RMS Height, Correlation Length	0.6cm*, 10.0cm*	0.6cm*, 10.0cm*	0.6cm*, 10.0cm*	0.6cm*, 10.0cm*
Bottom Surface RMS Height, Correlation Length	0.7cm*, 10.0cm*	0.7cm*, 10.0cm*	0.8cm*, 10.0cm*	0.8cm*, 10.0cm*

\+ denotes averaged value
* denotes estimated value

LIST OF PUBLICATIONS

Lum, C.-F., Ewe, H.-T., Fu-Xin and Jiang, L.-J., 2015. A study of single scattering of scatterer at various orientation angles with equivalence principle algorithm. *2015 10th International Conference on Information, Communications and Signal Processing (ICICS)*. December 2015 IEEE, pp. 1–4.

Lum, C.-F, Xin, F., Ewe, H. and Jiang, L., 2015. A Study of Scattering of Scatterers Using Equivalence Principle Algorithm. *PIERS Proceedings*, pp. 1897–1900.

Lum, C.-F., Fu Xin, Ewe, H.-T. and Jiang, L.-J., 2016. A study of scattering from a layer of random discrete medium with Hierarchical Equivalent Source Algorithm (HESA). *2016 Progress in Electromagnetic Research Symposium (PIERS)*. August 2016 IEEE, pp. 2545–2547.

Lum, C.-F., Fu, X., Ewe, H.-T. and Jiang, L.J., 2017. A study of scattering from snow embedded with non-spherical shapes of scatterers with relaxed hierarchical equivalent source algorithm (RHESA). *Progress In Electromagnetics Research M*, 61, pp.51–60.